

Diapycnal Displacement, Diffusion, and Distortion of Tracers in the Ocean

HENRI F. DRAKE, A XIAOZHOU RUAN, AND RAFFAELE FERRARI

^a MIT-WHOI Joint Program in Oceanography, Applied Ocean Science and Engineering, Cambridge and Woods Hole, Massachusetts ^b Department of Earth, Atmospheric, and Planetary Sciences, Massachusetts Institute of Technology, Cambridge, Massachusetts

(Manuscript received 13 January 2022, in final form 11 August 2022)

ABSTRACT: Small-scale mixing drives the diabatic upwelling that closes the abyssal ocean overturning circulation. Indirect microstructure measurements of in situ turbulence suggest that mixing is bottom enhanced over rough topography, implying downwelling in the interior and stronger upwelling in a sloping bottom boundary layer. Tracer release experiments (TREs), in which inert tracers are purposefully released and their dispersion is surveyed over time, have been used to independently infer turbulent diffusivities—but typically provide estimates in excess of microstructure ones. In an attempt to reconcile these differences, Ruan and Ferrari derived exact tracer-weighted buoyancy moment diagnostics, which we here apply to quasi-realistic simulations. A tracer's diapycnal displacement rate is exactly twice the tracer-averaged buoyancy velocity, itself a convolution of an asymmetric upwelling/downwelling dipole. The tracer's diapycnal spreading rate, however, involves both the expected positive contribution from the tracer-averaged in situ diffusion as well as an additional nonlinear diapycnal distortion term, which is caused by correlations between buoyancy and the buoyancy velocity, and can be of either sign. Distortion is generally positive (stretching) due to bottom-enhanced mixing in the stratified interior but negative (contraction) near the bottom. Our simulations suggest that these two effects coincidentally cancel for the Brazil Basin Tracer Release Experiment, resulting in negligible net distortion. By contrast, near-bottom tracers experience leading-order distortion that varies in time. Errors in tracer moments due to realistically sparse sampling are generally small (<20%), especially compared to the $\mathcal{O}(1)$ structural errors due to the omission of distortion effects in inverse models. These results suggest that TREs, although indispensable, should not be treated as "unambiguous" constraints on diapycnal mixing.

KEYWORDS: Diapycnal mixing; Diffusion; Upwelling/downwelling; Bottom currents/bottom water; Tracers

1. Introduction

The lower limb of the ocean's meridional overturning circulation traces the diabatic life cycle of abyssal bottom waters (Talley 2013), which store vast quantities of climatically active tracers like heat and carbon. Bottom waters are formed at the surface of the Southern Ocean by atmospheric cooling and brine rejection and are consumed in the abyssal ocean by buoyancy-flux convergence due to small-scale mixing and geothermal heating (Abernathey et al. 2016; de Lavergne et al. 2016b). Since mixing processes are too small to be resolved by large-scale ocean models, the rate at which tracers are mixed across density surfaces—the diapycnal diffusivity—enters as a key free parameter in ocean and climate models (Bryan and Lewis 1979; Simmons et al. 2004; de Lavergne et al. 2020). While early models of the abyssal circulation assume this

Drake's current affiliation: Geophysical Fluid Dynamics Laboratory, Princeton University, Princeton, New Jersey.

Corresponding author: Henri F. Drake, henrifdrake@gmail.com

mixing to be spatially uniform (Munk 1966; Stommel and Arons 1959), subsequent in situ observations reveal a complex geography of mixing processes (e.g., Polzin et al. 1997; Waterhouse et al. 2014). A robust pattern that emerges from these in situ mixing observations is the bottom enhancement of mixing over rough topography, consistent with theoretical arguments that this mixing is predominantly caused by breaking internal waves radiating from flow over topography (Munk and Wunsch 1998; Polzin 2009; Nikurashin and Ferrari 2010; Nikurashin and Legg 2011; MacKinnon et al. 2017; Whalen et al. 2020).

The observed bottom enhancement of deep mixing demands a revision of classic abyssal circulation theory: in the stratified interior, bottom-enhanced mixing above rough topography results in a layer of buoyancy flux divergence—the downwelling stratified mixing layer (SML)—and a thin layer of even larger buoyancy flux convergence at the insulating¹

¹ Geothermal heat flux into the BBL acts to amplify upwelling but is thought to be secondary to mixing globally (de Lavergne et al. 2016a) and is negligible in the Brazil Basin subregion considered here (Thurnherr et al. 2020).

seafloor—the upwelling bottom boundary layer (BBL). These ideas were first introduced at the regional scale in the Brazil Basin (Polzin et al. 1997; Ledwell et al. 2000; St. Laurent et al. 2001; Huang and Jin 2002) and then generalized to the global context (Ferrari et al. 2016; de Lavergne et al. 2016b; McDougall and Ferrari 2017; Callies and Ferrari 2018): the global diabatic overturning circulation is the small residual of substantial downwelling in the SML and even larger upwelling in the BBL (Drake et al. 2020). While the existence of these upwelling/downwelling flows is virtually guaranteed by the combination of a bottom-enhanced turbulent buoyancy flux and an insulating boundary condition along a sloping seafloor, the structure, magnitude, and underlying dynamics of these flows remain poorly understood (see Drake 2021; Polzin and McDougall 2022). Since diapycnal (or vertical) velocities and fluxes are challenging to directly measure [and interpret—see Polzin et al. (2021) for a recent example], bulk methods, such as volume or buoyancy budgets (e.g., St. Laurent et al. 2001; Lele et al. 2021), are commonly used instead to indirectly infer the flow. Water-mass transformation analysis (Walin 1982; Marshall et al. 1999) is a commonly used framework which combines volume and buoyancy budgets to express diapycnal transport across a buoyancy surface in terms of the average turbulent buoyancy flux convergence along the surface (de Lavergne et al. 2016b; Ferrari et al. 2016), which can be inferred from indirect observations (Spingys et al. 2021).

There are several observational methods for indirectly estimating in situ turbulent buoyancy fluxes and their corresponding diffusivities (listed roughly in order of decreasing accuracy and generality; see Gregg et al. 2018):

- 1) velocity shear microstructure ϵ , based on an approximate turbulent kinetic energy budget (Osborn 1980);
- 2) temperature variance microstructure χ , based on an approximate temperature variance budget (Osborn and Cox 1972);
- 3) scaling analysis, e.g., assuming the Thorpe scale L_T of density overturns approximates the Ozmidov scale L_O (Thorpe 1977; Dillon 1982; Mashayek et al. 2021); and
- 4) shear/strain variance finestructure $\epsilon_{\rm IW}$, based on idealized spectral models of internal wave dynamics (e.g., Garrett and Munk 1972, 1975; Henyey et al. 1986; Gregg 1989; Polzin et al. 1995; Gregg et al. 2003; Kunze et al. 2006; Dematteis and Lvov 2021).

All of these methods are indirect and require some degree of approximation to convert the measured quantity into an in situ diffusivity (see Taylor et al. 2019), e.g., $\kappa \equiv -\langle w'b' \rangle/\langle b_z \rangle \simeq 0.2 \epsilon/\langle b_z \rangle$ (Osborn and Cox 1972). Furthermore, they provide only localized snapshots of spatially and temporally intermittent mixing events and thus may provide biased estimates of the *mean* diffusivity κ (Whalen 2021), which is often the goal of parameterization. How any of these estimates of vertical buoyancy fluxes or turbulent diffusivities relate to the three-dimensional divergence of the turbulent buoyancy flux (and thus the diapycnal velocity) is a major open question (Polzin and McDougall 2022).

Tracer (or dye²) release experiments (TREs; Watson and Ledwell 1988) are considered by many to provide the gold standard of mixing rate estimates. In TREs, an assumed inert chemical tracer is deliberately injected into the ocean and its distribution is surveyed by shipboard rosette sampling over time scales of months to years. The evolution of the tracer is then inverted (using approximate advection-diffusion models) to yield estimates of the mean diffusivity and velocity, which can be compared to independent in situ turbulence measurements. Localized TREs are experimental analogs of the mathematician's Green's function approach and are thus easier to interpret than thermodynamic or biogeochemical tracers with less well known initial or boundary conditions and more complicated dynamics and mixing histories (e.g., Hogg et al. 1982; Lumpkin and Speer 2007; Trossman et al. 2022). However, the results of the TRE inversion process depend crucially upon the assumptions made to infer diffusivities from approximate advection-diffusion forward models.

Watson and Ledwell (1988) pitch TREs in the ocean as an "unambiguous measure of the diapycnal mixing rate" since tracers average over the spatial and temporal variability that challenges the interpretation of in situ mixing estimates. For example, Watson and Ledwell (1988) hypothesize that the sparse sampling of log-normally distributed mixing events by in situ microstructure measurements risks systematically underestimating mean mixing rates (Baker and Gibson 1987). Superficially, observations from two deep-ocean TREs seem to corroborate this hypothesis: tracer-based estimates of mixing rates are ubiquitously 1.5-10 times larger than collocated in situ microstructure measurements (Ledwell et al. 2000; Watson et al. 2013; Mashayek et al. 2017). While there are ad hoc and site-specific explanations for each of these discrepancies, there is no consensus on how best to compare tracerbased and microstructure-based estimates (Gregg et al. 2018), nor what to make of the fact that tracer-based estimates seem to always exceed microstructure-based estimates.

Recent advances in the numerical modeling and theory of TREs provide some guidance for interpreting tracer-based estimates of mixing and comparing them to microstructure-based estimates. For example, Mashayek et al. (2017) use a realistic regional simulation to argue that the mixing inferred from the Diapycnal and Isopycnal Mixing Experiment in the Southern Ocean (DIMES) TRE (Watson et al. 2013) was an order of magnitude larger than the in situ diffusivity estimated from microstructure because the average diapycnal spreading of the tracer was dominated by a small fraction of the tracer distribution that resided in regions of relatively vigorous mixing near rough topography. By deriving an exact evolution equation for the second tracer-weighted buoyancy moment, Holmes et al. (2019) confirm Mashayek et al.'s (2017) speculation that a tracer's buoyancy variance grows (in part) like the

² Fluorescent dye can be used for time scales of hours to days and can be sampled as much higher resolution with in situ fluorometers (e.g., Ledwell et al. 2004), or—for near-surface releases—remote sensing instruments (Sundermeyer et al. 2007).

³ Cael and Mashayek (2021) argue that these biases may be even larger because turbulence distributions are log-skew normal.

tracer-weighted in situ diffusivity. Ruan and Ferrari (2021) present a more intuitive from of these equations, which allows them to clearly identify an additional "diapycnal distortion" term through which the bottom enhancement of mixing in the SML induces "diapycnal stretching" that further accelerates the diapycnal spreading of the tracer. Holmes et al. (2019) demonstrate that this diapycnal stretching in the SML is somewhat compensated for by a "boundary suppression" (or, more generally, "diapycnal contraction") effect due to upwelling of relatively dense tracer in the sloping BBL. Since both of these analyses rely on extremely idealized models, it remains unclear to what extent diapycnal distortion affects tracers in realistic conditions (e.g., eddying three-dimensional flows over rough topography). Previous observational studies have speculated about the qualitative impacts of these distortion effects (Ledwell and Hickey 1995; Ledwell et al. 2000), but did not discuss whether their inverse models account for this distortion.

In this paper, we apply Ruan and Ferrari's (2021) tracer-weighted buoyancy moments method to quasi-realistic TRE simulations. We use these diagnostics to reinterpret the diapycnal downwelling and spreading observed in the Brazil Basin TRE (Ledwell et al. 2000; St. Laurent et al. 2001) in the context of an emerging paradigm of bottom mixing layer control of the global abyssal circulation (Ferrari et al. 2016; McDougall and Ferrari 2017). We also provide guidance for the interpretation of past (e.g., Ledwell and Hickey 1995; Ledwell et al. 2004; Holtermann et al. 2012; Ledwell et al. 2016; Mackay et al. 2018; Visbeck et al. 2020) and future TREs in light of potentially significant diapycnal distortion.

2. Theory

We briefly review Ruan and Ferrari's (2021) recently proposed framework for comparing tracer-based and microstructure-based mixing estimates, based on exact evolution equations for tracer moments in buoyancy space. The derivation begins with the conservation equations for tracer concentration c and buoyancy b,

$$\frac{\partial c}{\partial t} + \mathbf{u} \cdot \nabla c = \nabla \cdot (\kappa \nabla c) \tag{1}$$

$$\frac{\partial b}{\partial t} + \mathbf{u} \cdot \nabla b = \nabla \cdot (\kappa \nabla b), \tag{2}$$

where \mathbf{u} is the velocity vector, $\nabla = (\partial/\partial x, \partial/\partial y, \partial/\partial z)$ is the gradient operator, and κ is an isotropic turbulent diffusivity (assumed to be the same for all tracers). Buoyancy, tracer concentrations, and velocity have been filtered on spatial and temporal scales larger than those associated with small-scale turbulence (De Szoeke and Bennett 1993). For any filtered scalar ϕ , turbulent fluxes are parameterized as an enhanced diffusive flux $\mathbf{F}_{\phi} = -\kappa \nabla \phi$, where the effective turbulent diffusivity κ is assumed isotropic and much larger than the molecular diffusivity. For simplicity of exposition, we here approximate density as a linear function of temperature; thus, buoyancy b, density ρ , and temperature T are all proportional and will be used interchangeably throughout: $b \equiv -g(\rho/\rho_0) \approx g\alpha T$, where $\rho_0 = 1000 \text{ kg m}^{-3}$

is a reference density and $\alpha = 2 \times 10^{-4} \, ^{\circ}\text{C}^{-1}$ is the thermal contraction coefficient.

a. Exact tracer-weighted buoyancy moment models

In his classic paper, Taylor (1922) demonstrates that half the growth rate of a one-dimensional (1D) tracer distribution's variance is exactly equal to the diffusivity acting upon it. Ruan and Ferrari (2021) generalize this theory to the case of variable diffusivity in a stably stratified fluid by considering moments in buoyancy space. By cross multiplying the passive tracer (1) and buoyancy (2) equations and integrating over a volume $\mathcal V$ containing the tracer (or bounded by insulating and impermeable boundaries), they derive straightforward and exact evolution equations for the first and second tracerweighted buoyancy moments,

$$\partial_t \overline{T} = 2\overline{\omega} \quad \text{and}$$
 (3)

$$\frac{1}{2}\partial_t \overline{(T')^2} = \overline{\kappa |\nabla T|^2} + 2\overline{\omega' T'},\tag{4}$$

respectively, where overlines denote the tracer-weighted average, $\overline{\star} \equiv \int_{\mathcal{V}} \star c dV/\int_{\mathcal{V}} c dV$; primes denote variations from the tracer average, $\star' \equiv \star - \overline{\star}$; and $\omega \equiv \nabla \cdot (\kappa \nabla T)$ is the in situ buoyancy velocity, which is the magnitude of the diapycnal velocity through buoyancy space (e.g., Marshall et al. 1999). Following Ruan and Ferrari (2021), we take the optional step of converting the buoyancy moment tendencies to more intuitive physical units by normalizing with the appropriate tracer-weighted powers of the buoyancy gradient, bielding an effective diapycnal tracer velocity w_{Tracer} , and effective diapycnal tracer diffusivity κ_{Tracer} ,

$$w_{\text{Tracer}} \equiv \frac{\partial_t \overline{T}}{|\nabla T|} = \frac{2\overline{\omega}}{|\nabla T|} \quad \text{and}$$
 (5)

$$\kappa_{\text{Tracer}} \equiv \frac{1}{2} \frac{\partial_t \overline{(T')^2}}{|\nabla T|^2} = \underbrace{\frac{\overline{\kappa |\nabla T|^2}}{|\nabla T|^2}}_{\substack{\kappa_{\text{Taylor}} \\ \text{diffusion}}} + \underbrace{2 \frac{\overline{\omega' T'}}{|\nabla T|^2}}_{\substack{\kappa_{\omega} \\ \text{(distortion)}}}.$$
 (6)

The primary goal of many TREs is to verify uncertain in situ estimates of the mixing rate κ (the right-hand sides), with more reliable in situ measurements of T and c (the left-hand sides). Assuming, for example, that correlations between κ and $|\nabla T|$ and between ω are T are small, we recover an equation similar to Taylor's (1992) classic result that in situ mixing

⁴ Holmes et al. (2019) present similar exact equations but do not recognize that all of the terms can be expressed exactly in terms of tracer-weighted averages. Furthermore, many of their manipulations rely on unnecessary assumptions (e.g., the normalization by a constant background stratification N^2 in their section 6a) or are not applicable to our rough topography context (e.g., their discussion of boundary effects in their section 6b).

⁵ Unlike Ruan and Ferrari (2021), we do not approximate the buoyancy gradients by ignoring horizontal components, so our equations are exact.

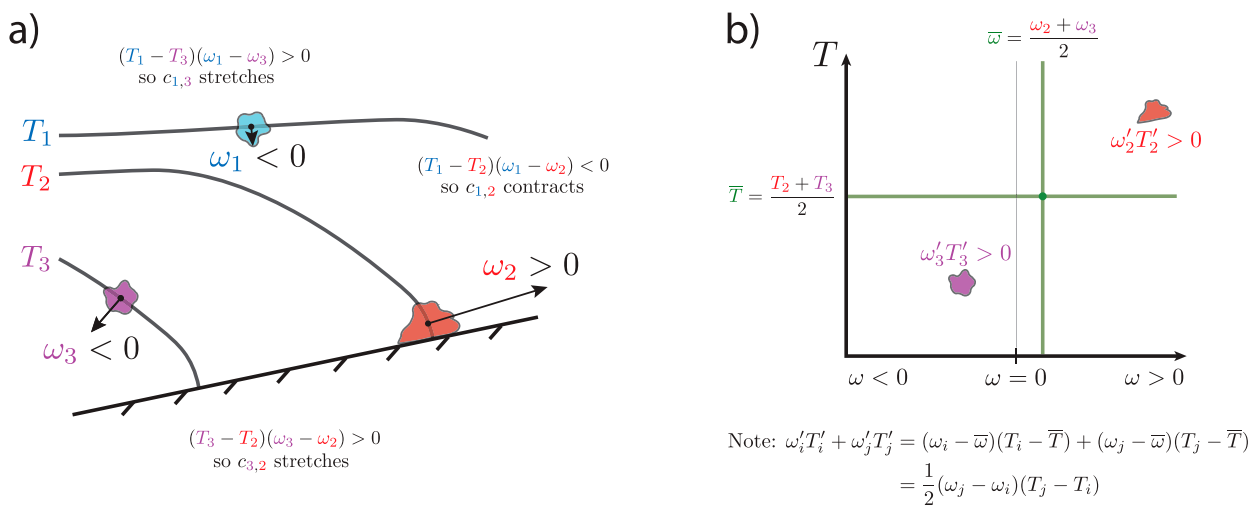


FIG. 1. Examples of diapycnal distortion of idealized dipole tracer distributions [Eq. (8)] (a) in physical space and (b) in (ω, T) space, motivated by the quasi-realistic simulation results in section 4. In (a), the three tracer distributions $c_{1,3}$, $c_{1,2}$, and $c_{3,2}$ experience diapycnal stretching or contraction effects due to temperature and buoyancy velocity differences. Gray lines show the equally spaced temperature surfaces corresponding to the three tracer patches. Arrows represent the magnitude of the buoyancy velocity ω and are oriented normal to temperature surfaces. In (b), a PDF of contributions to the $c_{3,2}$ net diapycnal distortion effects for both tracer patches (see section 4d) is shown. Olive lines mark the average buoyancy velocity and temperature of the tracer.

rates can be directly diagnosed from the tendencies of the two tracer-weighted buoyancy moments:

$$\overline{\kappa} \simeq \frac{1}{2} \frac{\partial_t (\overline{T'})^2}{|\nabla T|^2}.$$
 (7)

b. Interpreting the tracer-weighted buoyancy moments

Consider the extreme example of a dipole tracer distribution $c_{i,j}$, consisting of two infinitesimal patches of equal mass at locations \mathbf{x}_i and \mathbf{x}_j ,

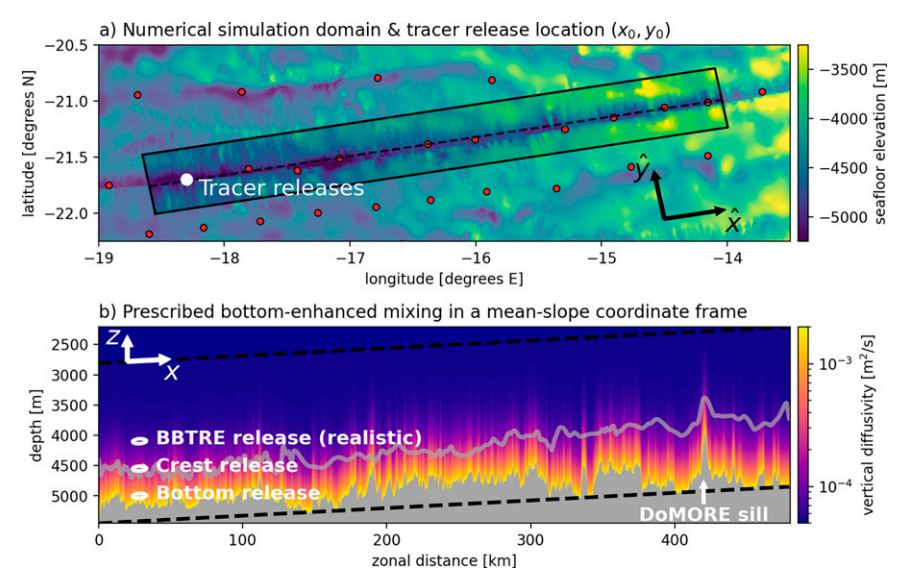


FIG. 2. Numerical model configuration: domain geometry, prescribed forcing, and key features. (a) Rectangular domain (solid lines) centered along the BBTRE canyon thalweg (dashed line) and interpolated onto locally tangent cartesian coordinates (\hat{x}, \hat{y}) Red dots mark the stations where the BBTRE tracer was sampled. (b) Prescribed bottom-enhanced mixing (colors) along the canyon thalweg (gray shading). Dashed black lines show the domain limits in the slope-native coordinate frame (x, z). The transparent gray line shows the average height of the canyon crests, which rise 500–1000 m above the thalweg (its deepest section). White dots/contours show the locations of the simulated tracer releases. The location of the prominent Dynamics of the Mid-Ocean Ridge Experiment (DoMORE; see Clément et al. 2017) sill is shown for reference.

$$c_{i,j}(\mathbf{x}) = \frac{\delta(\mathbf{x}_i) + \delta(\mathbf{x}_j)}{2},$$
 (8)

where $\delta(\mathbf{x})$ is the delta function and the entire tracer distribution has unit mass, $\int_{\mathcal{V}} cdV = 1$. Evaluating the terms in the tracer-weighted first buoyancy moment evolution Eq. (3) for this hypothetical tracer distribution (8), we find that the tracer warms on average at a rate of twice the average buoyancy velocity of the two patches,

$$\partial_t \overline{T} = 2\overline{\omega} = \omega_i + \omega_i, \tag{9}$$

where we use the shorthand $\phi_k = \phi(\mathbf{x}_k)$. The tendency of the tracer's centered second buoyancy moment (4) is, after some algebra (e.g., expanding and refactoring terms with $\phi'_i = \phi_i - \overline{\phi} = \overline{\phi} - \phi_i$),

$$\frac{1}{2}\partial_{t}\overline{(T')^{2}} = \overline{\kappa |\nabla T|^{2}} + \frac{1}{2}\Delta\omega\Delta T, \tag{10}$$

where $\Delta\omega\equiv\omega_j-\omega_i$ and $\Delta T\equiv T_j-T_i$ are buoyancy velocity and temperature differences between the two patches, respectively. While the first moment tendency is simply given by the average of the two patches' tendencies, the centered second moment tendency includes an additional nonlinear distortion term. If the warmer patch upwells faster than the colder patch $(\Delta\omega\Delta T>0)$, this term drives diapycnal stretching (e.g., $c_{1,3}$ and $c_{3,2}$ in Fig. 1); conversely, $\Delta\omega\Delta T<0$ corresponds to diapycnal contraction (e.g., $c_{1,2}$ in Fig. 1).

A corollary of (10) is the fact that estimates of the in situ diffusivity are most reliable when the injected tracer distribution is compact in buoyancy space (i.e., small ΔT), lending support to the practice of making tracer injections as compact in buoyancy space as possible. Even for an initially compact tracer injection with small $\Delta\omega\Delta T$, however, diapycnal distortion may become significant over time as ΔT increases due to diapycnal diffusion. On the other hand, while isopycnal stirring does not increase ΔT (by definition), it can increase $\Delta\omega$ by distributing tracer into regions with varying buoyancy velocities (see Holmes et al. 2019). While the former effect is likely to be well represented in 1D advection–diffusion models used to interpret TRE data, the latter is not.

3. Numerical methods overview: Simulated tracer release experiments

We configure the MITgcm to simulate mixing-driven flow in the Brazil Basin TRE (BBTRE) region (Fig. 2a). Inspired by sloping bottom boundary layer theory (reviewed by Garrett et al. 1993), the system is solved in a coordinate frame aligned with the mean Mid-Atlantic Ridge slope, as described in detail in a companion manuscript (Drake et al. 2022) and summarized in appendix A. The simulation is forced only by bottom-enhanced turbulent mixing, which controls diabatic tracer upwelling and spreading and is thought to provide much of the energy that drives subinertial abyssal flows. We

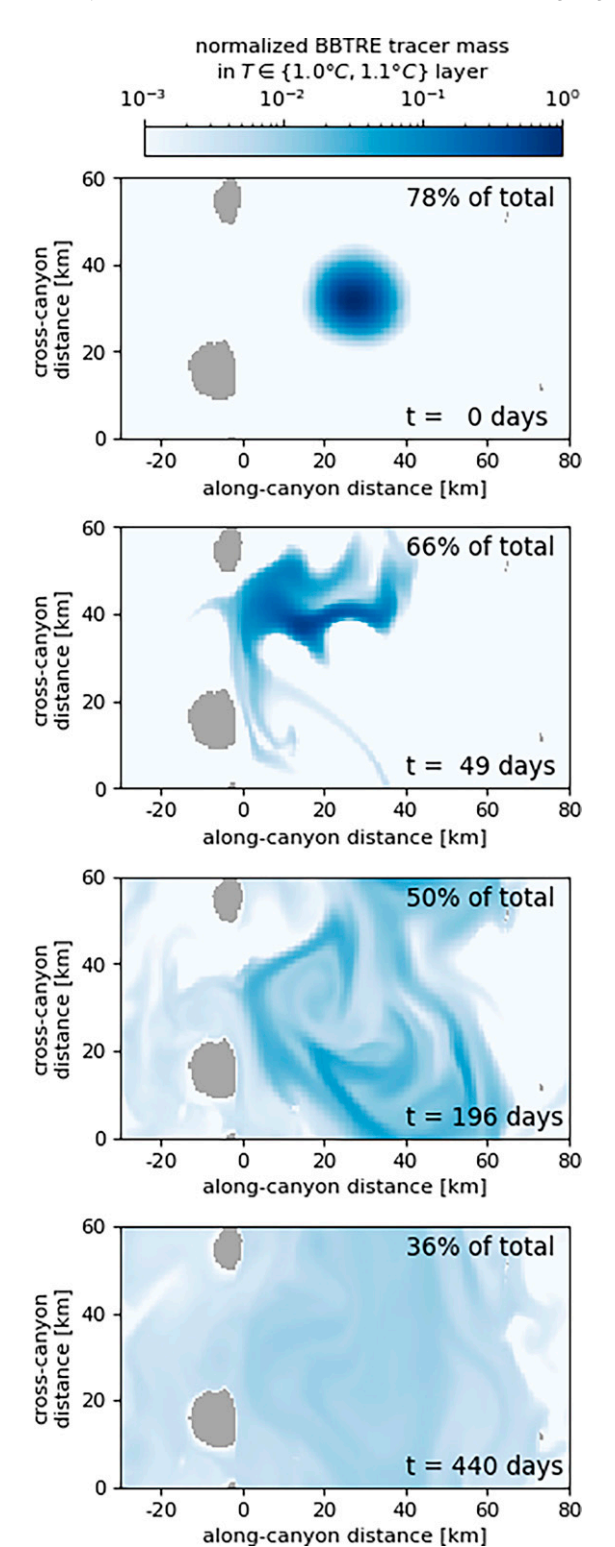


FIG. 3. Instantaneous snapshots of the BBTRE tracer mass, vertically integrated over the {1.0°, 1.1°C} temperature layer, and normalized by the maximum initial tracer mass. The fraction of the total tracer mass that remains in this layer is noted in the topright corner. The gray shading represents two major topographic obstacles, where the temperature layer intersects with the seafloor.

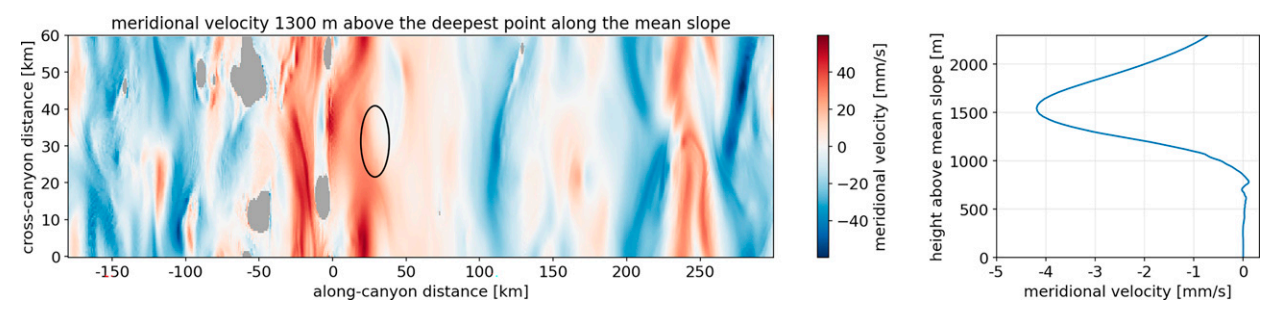


FIG. 4. (a) Cross-canyon (quasi-meridional) velocity v, 1300 m above the mean slope, i.e., at the release height of the BBTRE tracer. The black contour shows the initial extent of the tracers, which is released in an anomalously northward flow. (b) As in (a), but averaged across the whole domain.

impose a turbulent diffusivity κ that increases exponentially toward the seafloor at z = -d(x, y) (Fig. 2b),

$$\kappa(x, y, z) = \kappa(z; d) = \kappa_{\text{BG}} + \kappa_{\text{BOT}} \exp\left(\frac{z - d}{h}\right),$$

with parameters fit to the mean height-above-bottom microstructure profile in the region according to Callies (2018): $\kappa_{\rm BOT} = 1.8 \times 10^{-3} \ {\rm m^2 \ s^{-1}}, \ \kappa_{\rm BG} = 5.2 \times 10^{-5} \ {\rm m^2 \ s^{-1}}, \ {\rm and} \ h = 230 \ {\rm m}$

After spinning up the flow to a quasi-equilibrium state at t = 5000 days, we release three relatively small Gaussian blobs of tracer

$$c_n(x, y, z, t = 0) = c_0 \exp\left\{-\left[\frac{(x - x_0)^2}{2\sigma_x^2} + \frac{(y - y_0)^2}{2\sigma_y^2} + \frac{(z - z_n)^2}{2\sigma_z^2}\right]\right\},\tag{11}$$

with horizontal widths of $\sigma_x = \sigma_y = 3.5$ km, a thickness $\sigma_z = 28$ m, and horizontal release coordinates (x_0, y_0) corresponding to the location where the tracer was released in the BBTRE $(21.7^{\circ}\text{S}, 18.3^{\circ}\text{W})$ (Fig. 2). The tracers are released at three different heights z_n corresponding to distinct dynamically interesting regimes: far above the topography, $z_{\text{BBTRE}} + d(x_0, y_0) = 1050$ m above the seafloor (actual BBTRE release location; hereafter the BBTRE tracer); roughly at the height of the canyon crests, $z_{\text{Crest}} + d(x_0, y_0) = 600$ m (Crest); and within the thick BBL of the canyon trough, $z_{\text{Bottom}} + d(x_0, y_0) = 150$ m (Bottom). We follow the evolution of these released tracers until $t_f = 440$ days after release, roughly corresponding to the first survey in the BBTRE at 14 months.

4. Results

a. Temporal evolution of the released tracer distributions

Within the first few eddy turnover time scales, the released tracer blobs are stirred into a web of filaments along isopycnals by submesoscale eddies (Fig. 3). While the BBTRE and Crest tracers are released well above the canyon thalweg (its deepest section; Fig. 2a), vigorous along-ridge mean flows (Fig. 4) and isopycnal stirring by submesoscale eddies spread them to shallower regions (Fig. 5). Spreading rates in the up-canyon direction, over the length of the

experiments, are $K^{(x)} \equiv (1/2)[\overline{\Delta(x')^2}/\Delta t] \simeq 10 \text{ m}^2 \text{ s}^{-1}$ for the BBTRE tracer—the sequence of snapshots in Fig. 3 suggests this is largely due to submesoscale eddy stirring. The Bottom and Crest releases experienced more rapid spreading of $\mathcal{O}(30)$ m² s⁻¹, likely due to the additional shear dispersion (Taylor 1953) by the bidirectional along-canyon mean flows (Figs. 5i,j).

The tracers are diffused diapycnally by the prescribed bottom-enhanced turbulent mixing (e.g., Figs. 5b,d). For the BBTRE tracer, which mostly remains well above the bottom, its distribution in temperature space remains reasonably Gaussian (Fig. 5d), reminiscent of diffusion with a constant diffusivity and in the absence of boundaries. For the Crest and Bottom tracers, however, the tracer distributions depart significantly from Gaussianity (Figs. 5h,l), suggesting the importance of variations in the diffusivity or boundary effects (Holmes et al. 2019). Most notably, the Bottom tracer develops a bimodal distribution in temperature space as some of the tracer spills over the minor sill at x = 120 km and crosses the T = 0.7°C surface (Figs. 5j,1). By the end of the experiment at 440 days, most of the Bottom tracer has spilled over the sill and its bimodal distribution collapses onto a single, warmer peak. While only the Bottom tracer exhibits a tracer-weighted diapycnal displacement that is discernible by visually inspecting the tracer distributions in temperature space, the BBTRE and Crest tracers do exhibit slow mean diapycnal downwelling and upwelling, respectively.

Diapycnal interior downwelling and boundary upwelling driven by bottom-enhanced mixing

As described in section 2a, the tracer's center of mass \overline{T} is displaced at a rate of *twice* the tracer-weighted buoyancy velocity $\overline{\omega} \equiv \overline{\nabla \cdot (\kappa \nabla T)}$ [Eq. (3)]; the factor of two⁶ arises

⁶ Ledwell et al. (1998) attempt to compare an estimate of the left-hand side of (5) from a TRE with an estimate of the right-hand side based on St. Laurent and Schmitt's (1999) microstructure analysis; however, they appear to have erroneously omitted the factor of 2 in the first moment Eq. (5), which would have made the two estimates even more consistent. This example highlights the importance of rigorously deriving the physical models used to interpret TRE observations.

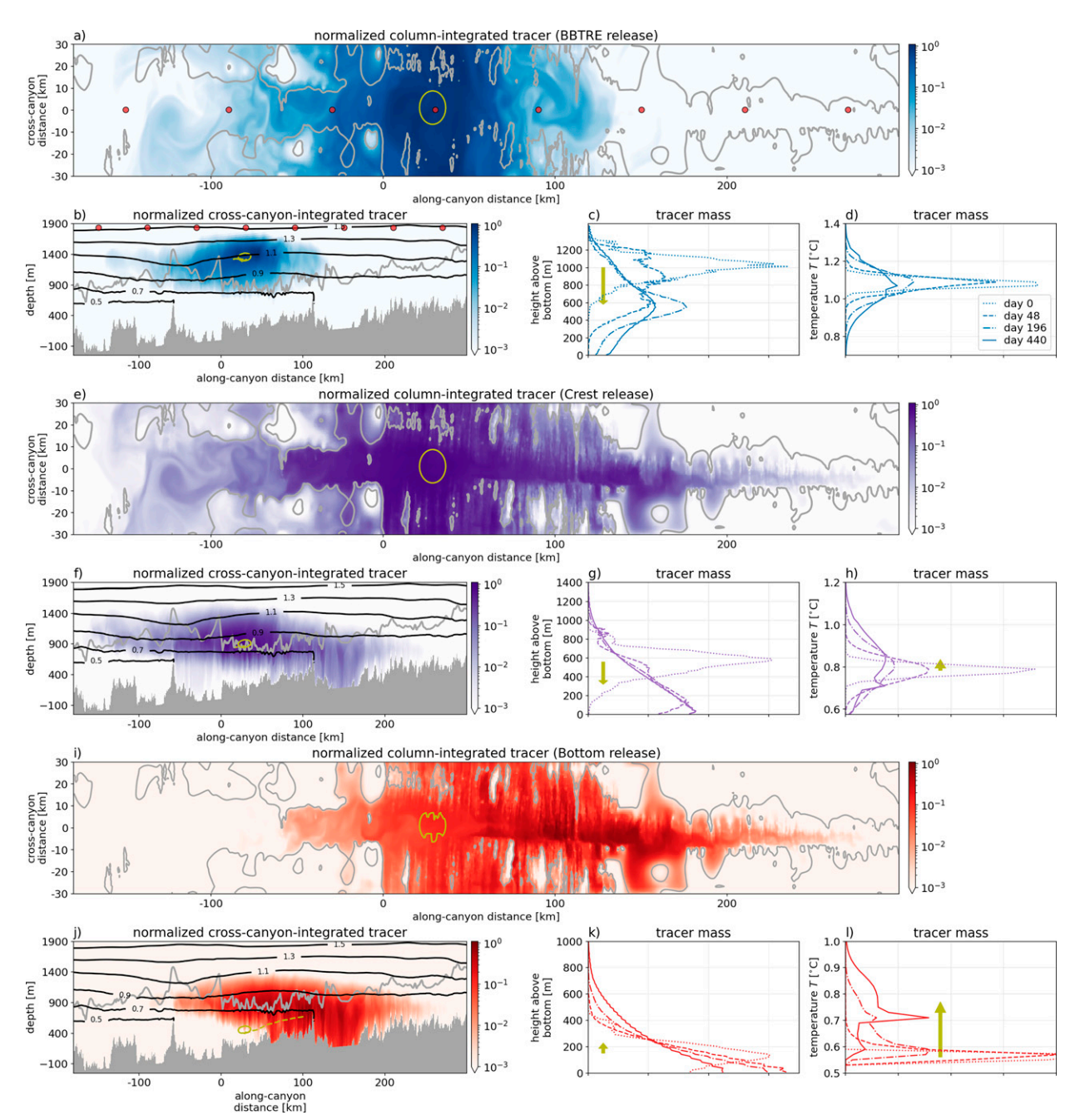


FIG. 5. Temporal evolution of the tracer distributions in Cartesian, height-above-bottom, and temperature coordinates for the (a)–(d) BBTRE (blues), (e)–(h) Crest (purples), and (i)–(l) Bottom releases (reds). Slope-normal column-integrated tracer concentrations in (a), (e), and (i) and cross-canyon-integrated tracer concentrations in (b), (f), (j) are shown 440 days after release and normalized by their instantaneous maximum value (logarithmic scale). Gray contours in (a), (e), and (i) show two representative isobaths of ocean depth $\hat{d}(\hat{x},\hat{y})$ Black lines in (b), (f), and (j) show equally spaced cross-canyon-averaged temperature surfaces. Colored lines show normalized tracer distributions in height-above-bottom coordinates in (c), (g), and (k) and temperature coordinates in (d), (h), and (l). Olive contours show the 10% contour for the initial tracer distributions; olive dashed lines and arrows show the temporal evolution of the tracer's center of mass (first moment) in the various coordinate frames from day 0 to 440. Red dots in (a) and (b) mark the locations used in the hypothetical sampling survey discussed in section 4e.

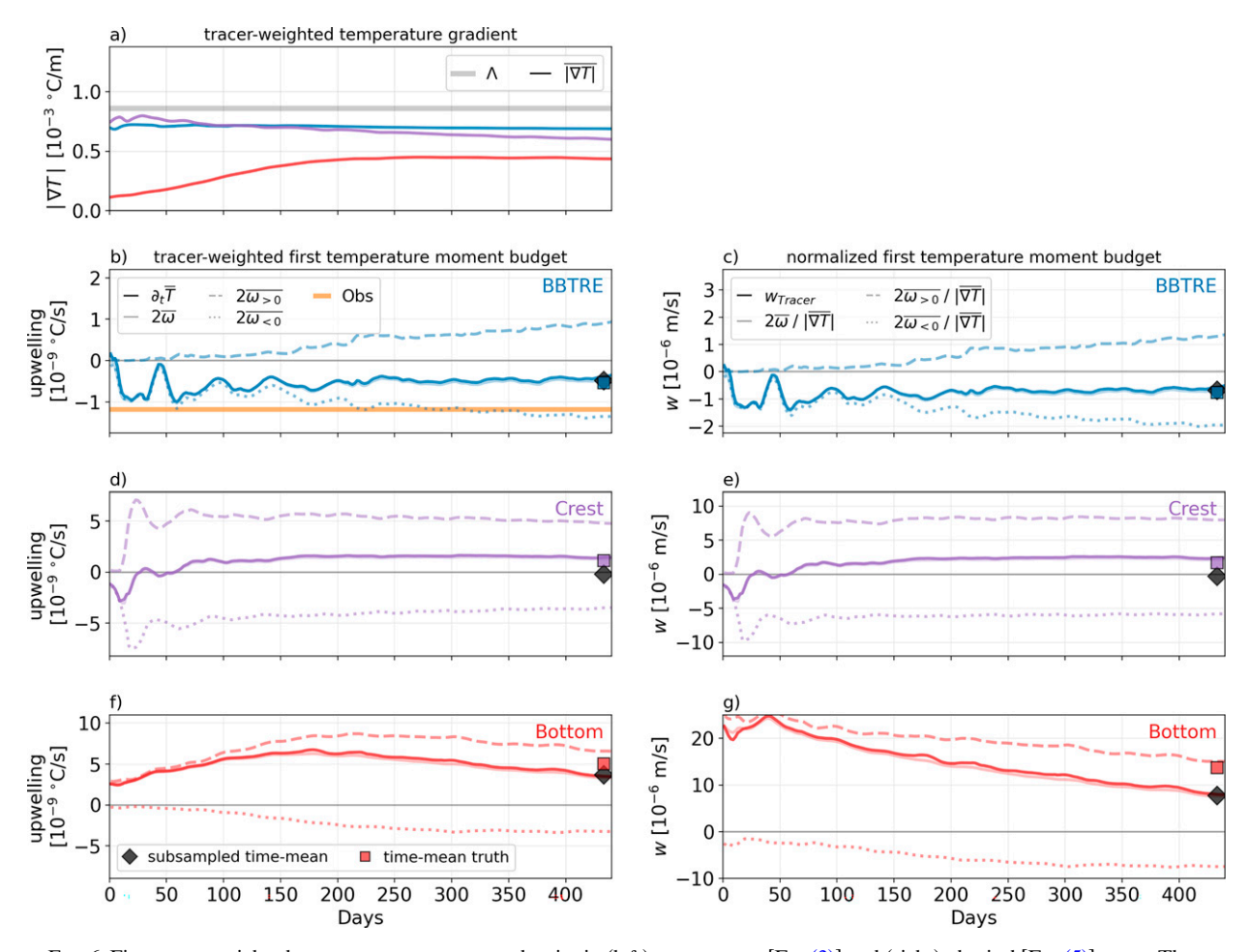


FIG. 6. First tracer-weighted temperature moment tendencies in (left) temperature [Eq. (3)] and (right) physical [Eq. (5)] space. The realistic BBTRE release is shown in blue, the Crest release in purple, and the Bottom release in red. (a) The temporal evolution of the tracer-weighted stratification, with the background stratification $\Lambda \equiv (dT_b/d\hat{z})$ for reference (see appendix A). (b)–(g) The temporal evolution (opaque solid lines) of the first moment tendencies, which are visually indistinguishable from the mixing-driven buoyancy velocities that cause them (transparent solid lines; demonstrating that spurious numerical mixing is negligible). Dashed and dotted lines show the contributions from strictly upwelling and strictly downwelling regions, respectively. The orange line in (b) shows the time-averaged BBTRE moment tendencies estimated from observations (Ledwell et al. 1998, revised by J. R. Ledwell 2022, unpublished manuscript). Colored squares mark the time-mean, while the black diamonds mark the estimate of the time-mean from a realistically sparse subsampling of the simulated data (see section 4e).

because buoyancy diffuses through tracer space in addition to tracer diffusing through buoyancy space (Ruan and Ferrari 2021). Well above the seafloor, the bottom enhancement of the diffusivity κ dominates the buoyancy velocity, resulting in diapycnal downwelling, $\omega < 0$, in a layer we thus define as the SML. Closer to the seafloor, the temperature flux must vanish to satisfy the insulating bottom boundary condition, i.e., $\mathbf{n} \cdot (-\kappa \nabla T) = 0$, where \mathbf{n} is normal to the boundary, resulting in vigorous diapycnal upwelling, $\omega > 0$, in a layer we define as the BBL (see Ferrari et al. 2016).

The BBTRE tracer, which is released in the SML, exhibits diapycnal downwelling throughout the experiment (Fig. 6b), consistent with the above phenomenology. The magnitude of downwelling, however, is modulated by a 45-day damped oscillation due to along-ridge advection by a mean flow of speed

 $U \approx 15 \text{ mm s}^{-1}$ (Fig. 4a) across a periodic domain of width $L_y = 60 \text{ km}$. Following a depth surface, the bulk of the tracer thus aliases the canyon's trough–crest topography on a time scale of $\tau = L_y/U \approx 45 \text{ days}$, oscillating between weak diapycnal downwelling when well above the canyon floor and, because of the bottom-enhanced diffusivity profiles, exponentially stronger downwelling when it passes over the shallower hills surrounding the canyon. This modulation is damped over time as the tracer spreads isopycnally and spans a region wider than the typical trough–crest separation (Fig. 5a).

In the first 100 days, interpreting the mean diapycnal sinking of the BBTRE tracer is straightforward: the entire tracer distribution experiences a negative buoyancy velocity and so the tracer sinks diapycnally (Fig. 6b), i.e., $\overline{\omega} \approx \overline{\omega_{<0}}$, where we define

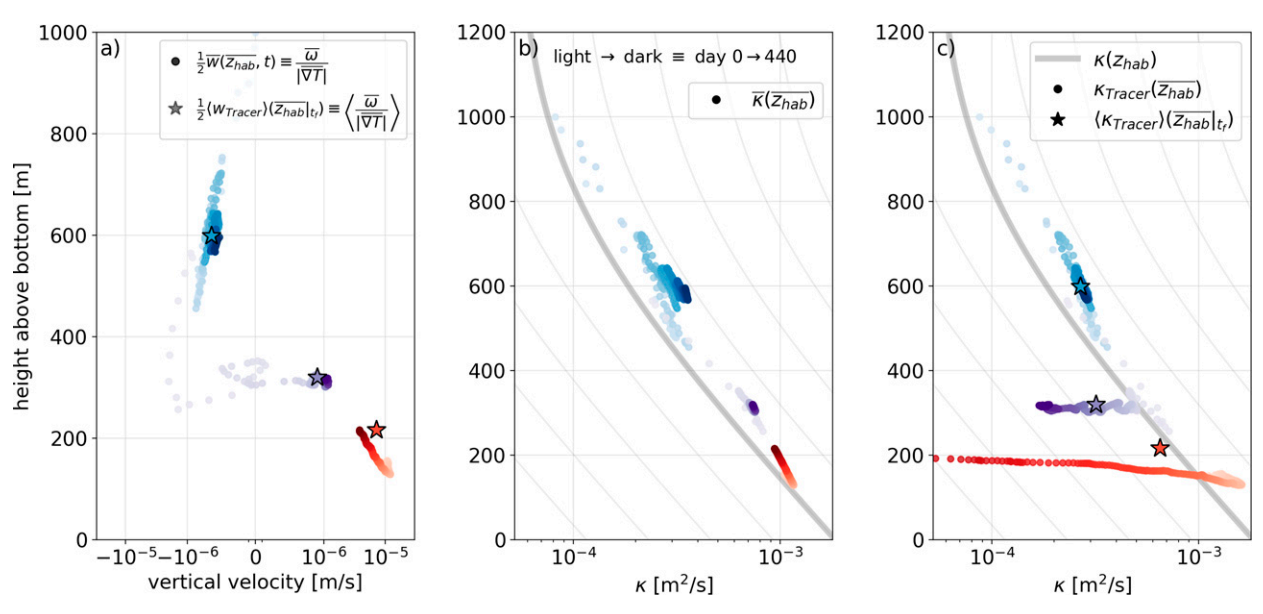


FIG. 7. (a) Tracer-weighted-average buoyancy velocities, normalized by the temperature gradient to yield an effective vertical velocity, as a function of tracer-weighted-average height above bottom $\overline{z_{\text{hab}}}(t)$ (colors). The effective tracer diapycnal velocity is divided by 2 to yield an estimate of the in situ diapycnal velocity $\omega/|\nabla T|$ (b),(c) As in (a), but for the tracer-weighted in situ diffusivity $\overline{\kappa}$ [Eq. (14)] and effective tracer diffusivity κ_{Tracer} [Eq. (6)]. The colored dots (BBTRE in blue; Crest in purple; Bottom in red) darken over time, from 0 to 440 days. Stars in (a) and (c) show estimates of the time-averaged terms based on a single tracer survey at 440 days and knowledge of the release temperature (see section 4e). The thick gray curves in (b) and (c) show the prescribed in situ diffusivity profile; thin gray lines show the profile multiplied by factors of 2^n .

$$\overline{\omega_{<0}} \equiv \frac{\int_{\mathcal{V}_{\omega<0}} \omega c dV}{\int_{c} c dV}$$
 (12)

as the strictly downwelling contribution to the tracer-averaged buoyancy velocity. While this strictly downwelling contribution strengthens slightly over the remainder of the experiment as the tracer sinks toward larger diffusivities, sufficient tracer is entrained into the BBL that a strictly upwelling contribution $\overline{\omega_{>0}}$ (similarly defined) grows at an even faster rate, such that the net diapycnal sinking of the tracer $(\overline{\omega} = \overline{\omega_{>0}} + \overline{\omega_{<0}})$ weakens over the remainder of the experiment (Fig. 6b).

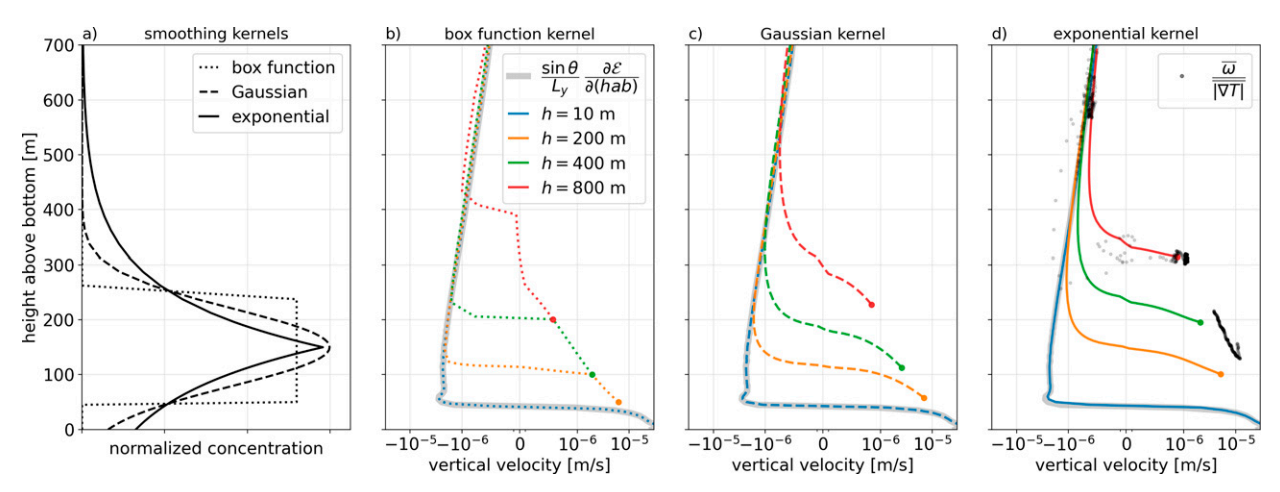


FIG. 8. Understanding the height-above-bottom structure of tracer transport by convolving the average velocity profile with idealized tracer kernels. (a) Three idealized shapes of tracer kernels, illustrated for a characteristic thickness of h = 200 m and centered at $\eta = 150$ m above the bottom. (b)–(d) Gray lines show the height-above-bottom averaged effective vertical velocity, estimated using water-mass transformation analysis [Eq. (B5)]. Colored lines show the result of convolving this profile with idealized kernels [Eq. (13)] of different shapes (columns), widths (colors), and heights above bottom η' (y axis). Black dots in (d) reproduce the snapshots of tracer-weighted buoyancy velocities shown in Fig. 7a, for reference.

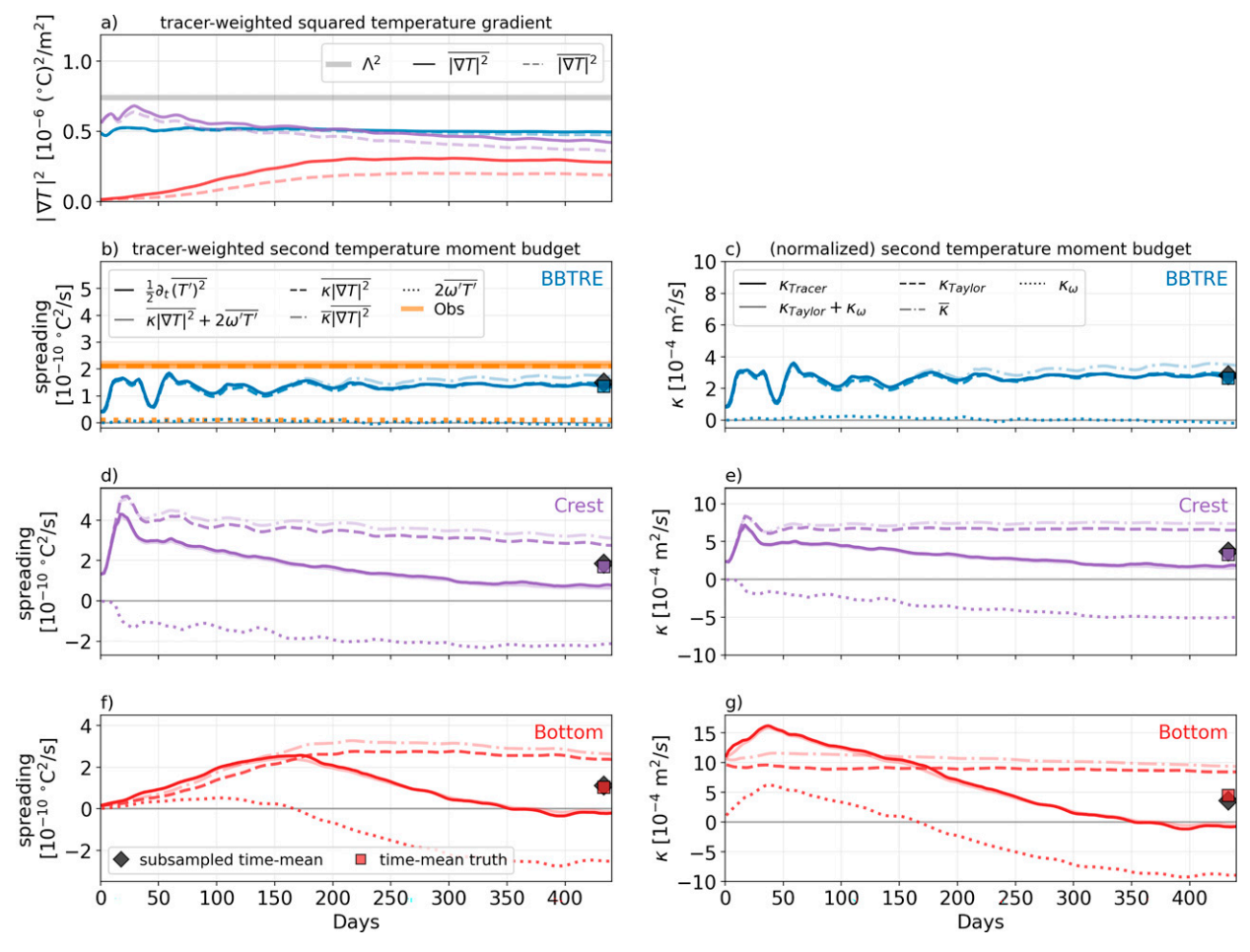


FIG. 9. As in Fig. 6, but for the tracer-weighted centered second-moment equations (4) and (6). Dash–dotted lines in (b)–(g) show the approximation of the diffusive term when correlations between κ and $|\nabla T|$ are ignored. Right-hand-side terms for the observations are estimated by applying the bottom-enhanced diffusivity profile that emerges from a 1D diffusion model (J. R. Ledwell 2022, unpublished manuscript); their sum is consistent with the left-hand side measured from the diapycnal tracer spreading.

At the other extreme, the Bottom tracer is released entirely in the BBL and thus upwells vigorously across isopycnals upon release, with $\overline{\omega} \approx \overline{\omega_{>0}}$, and apparently accelerates over the first 200 days (Fig. 6f). However, since the Bottom tracer is released near the bottom of a weakly stratified depression along the canyon thalweg, its average stratification increases dramatically over the first 200 days as it spreads to more stratified regions (Fig. 6a); thus, when normalizing by a factor $|\nabla T|^{-1}$ to convert to physical space [Eq. (5)], the tracer-averaged upwelling rate instead decreases monotonically over time due to both an increasing tracer-averaged stratification and an increasing contribution from tracer that has spread into downwelling regions (Figs. 6f.g).

The Crest release is perhaps the most interesting: at first, the Crest tracer is in the SML far above the canyon thalweg and thus downwells similarly to the BBTRE tracer; after roughly $\tau/2 = 23$ days, however, enough of the Crest tracer is advected into the BBLs along the rim of the canyon and the surrounding hills that the strictly upwelling component wins out and the tracer begins upwelling in the net (Figs. 6d,e).

Over the last few hundred days of the experiment, the weak net upwelling of the tracer is the small residual of a substantial compensation between strictly upwelling and strictly downwelling contributions.

By plotting the evolution of the tendency of the first temperature moment as a function of the tracer-weighted height above bottom [where $\eta \equiv z + d(x, y)$ is the height above bottom], we gain a qualitative sense of the height-above-bottom structure of the in situ buoyancy velocity $\omega/|\nabla T|$ (Fig. 7a). As the three tracers' centers of mass drift over time, their average buoyancy velocities trace out a diapycnal downwelling that intensifies rapidly toward the bottom in the SML (Fig. 7a, blue). Within about 300 m above the bottom, however, this downwelling gives way to upwelling (Fig. 7a, purple) which intensifies the closer the tracer is to the bottom (Fig. 7a, red).

Water-mass transformations provide a helpful reference for contextualizing the magnitude and vertical structure of tracer-weighted velocities. In appendix B, we convert the height-above-bottom (or η) structure of water-mass transformations

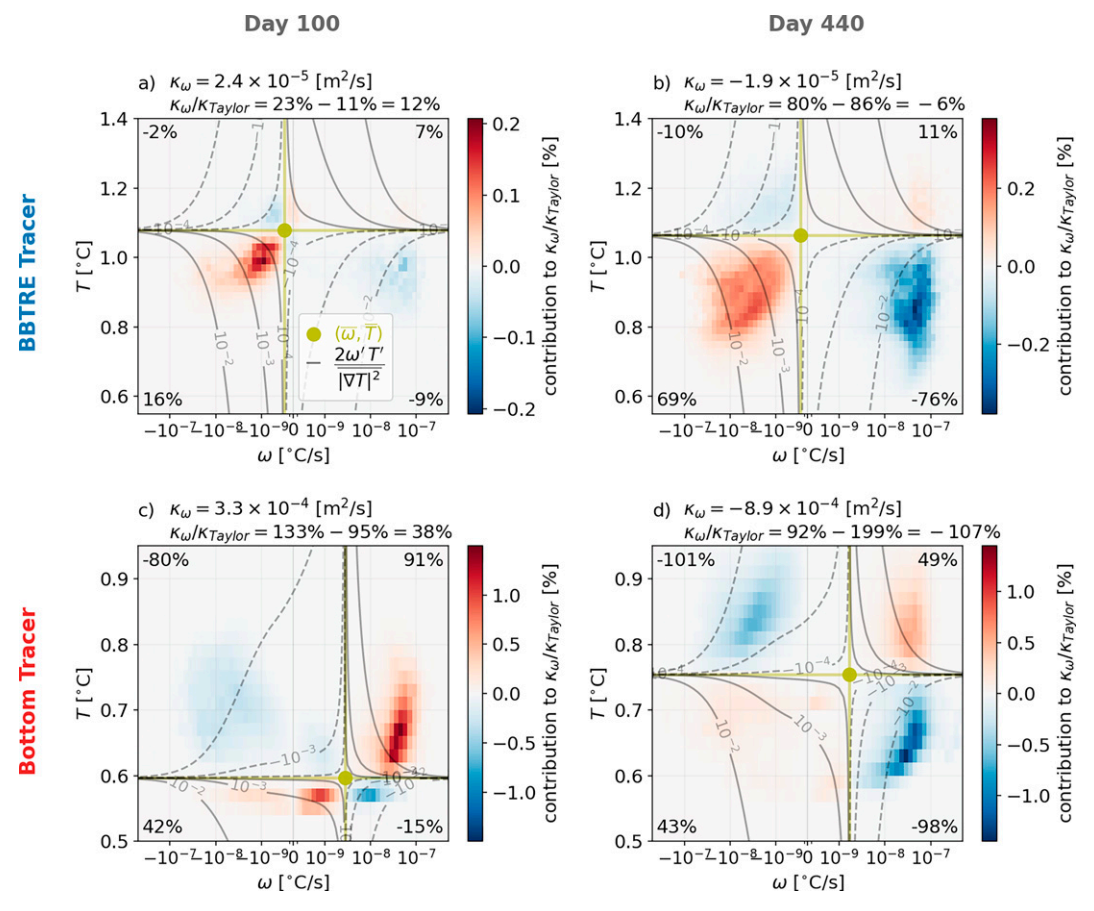


FIG. 10. Percentage contributions to the normalized net diapycnal distortion effect $\kappa_{\omega}/\kappa_{\rm Taylor}$ from each (ω,T) bin, as a percentage, for the (top) BBTRE and (bottom) Bottom tracers at (left) 100 days and (right) 440 days. The plotted quantity is the summand in Eq. (15), which is integrated such that the contributions from each bin (log-spaced in ω) can be visually and quantitatively compared. Numbers in the four corners of each panel show the summed contributions from each of the four quadrants delineated by the respective signs of $\omega' \equiv \omega - \overline{\omega}$ and $T' \equiv T - \overline{T}$. The $\omega' = 0$ and T' = 0 lines in olive delineate the four quadrants. For reference, gray contours show the effective diapycnal distortion diffusivity, $\kappa_{\omega} \equiv 2(\overline{\omega' T'}/|\nabla T|^2)$, that corresponds to each (ω,T) bin. Subtitles decompose the net diapycnal distortion effect into stretching $(\omega' T' > 0)$ and contracting components $(\omega' T' < 0)$.

into an effective vertical velocity versus η profile, $\overline{W}^I(\eta)$ [Eq. (B5); see appendix B]. This metric reveals that vigorous upwelling of $\mathcal{O}(4\times 10^{-5})\,\mathrm{ms}^{-1}$ is on average confined to the 40-m-thick BBL, largely compensated by downwelling that is an order of magnitude weaker—but also broader—in the SML above (Figs. 8b–d, gray lines). Superficially, this seems to be inconsistent with the tracer diagnostics which exhibit weaker upwelling over a much thicker layer (Fig. 8d, black dots).

The key to reconciling the two diagnostics is that the tracer distributions, while initially compact, rapidly spread in η space (Figs. 5c,g,k). To demonstrate the effect of this spreading on the tracer diagnostics, we convolve the vertical velocity versus η profile with smoothing tracer kernels of different shapes and widths (Fig. 8a),

$$\overline{W}(\eta) \approx \int_{-\infty}^{\infty} \mathcal{K}(\eta - \eta') \overline{W}^{T}(\eta') \ d\eta'. \tag{13}$$

Tracer kernels with widths less than the thickness of the BBL accurately reproduce the average η structure of water-mass transformations (Figs. 8b-d, blue lines), while thicker kernels begin convolving the BBL upwelling and SML downwelling together, reducing their magnitudes and elevating the apparent interface between them (Figs. 8b-d, other colors). This smearing effect of the convolution is particularly dramatic for exponential kernels with thick tails (Fig. 8d, green and red lines), which reasonably approximates the shapes of the Crest and Bottom tracers for most of the experiment (Figs. 5g,k). Indeed, convolving the vertical velocity η profile with exponential kernels of the same approximate width of these tracers roughly reproduces the tracer-diagnosed η structure of the buoyancy velocity (Fig. 8d). By contrast, the buoyancy velocity experienced by the BBTRE tracer is not as severely convolved (i.e., the dots near 600 m in Fig. 8d fall on the gray curve of the in situ buoyancy velocity) because the tracer remains sufficiently far above the bottom that it neither spreads as rapidly nor does it feel the compensating BBL upwelling (Fig. 5c).

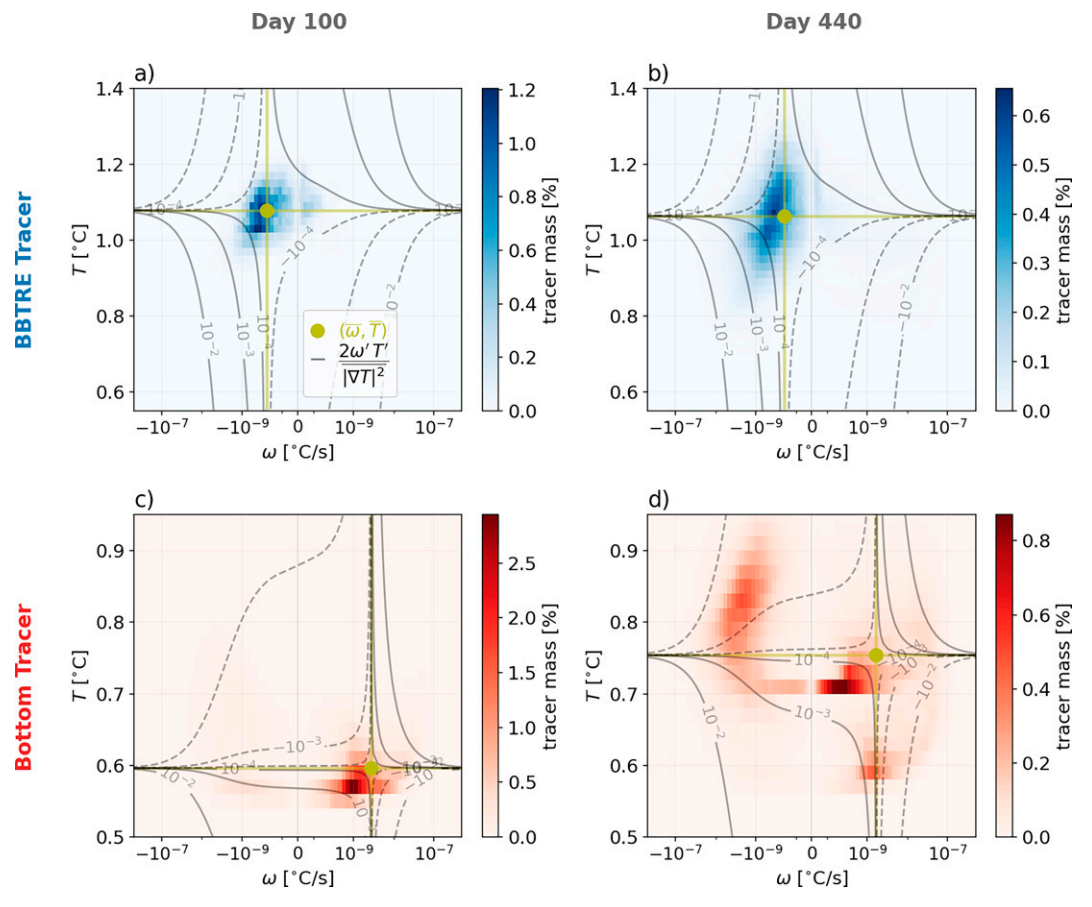


Fig. 11. Probability density function of tracer mass, as a percent contribution of each bin to the total tracer mass. Gray contours and olive lines as in Fig. 10. The distributions seem skewed relative to the means because of the log scale in ω .

c. Bottom-enhanced diapycnal tracer spreading

Over the course of the experiment, all three tracers spread across isopycnals on average. As anticipated from the prescribed bottom-enhanced diffusivity profile: the closer a tracer is released to the bottom, the faster it spreads (Fig. 7c; stars). However, this time-mean view obscures surprisingly large temporal variability (Fig. 9). This tendency is particularly dramatic for the Bottom tracer, which experiences extremely rapid diapycnal spreading in the first 150 days but, by day 350, stops spreading entirely and even begins temporarily contracting in temperature space (Figs. 9f,g)! The interpretation of diapycnal tracer spreading is more subtle than that of the mean diapycnal displacement of the tracer because two separate terms contribute to the spreading: the tracer-weighted effective diffusivity κ_{Taylor} and diapycnal distortion κ_{ω} [Eq. (6)]. The contribution from the tracer-weighted effective diffusivity is familiar from Taylor's (1922) classic derivation, and is reasonably well approximated by the tracer-weighted in situ diffusivity $\overline{\kappa}$ since correlations between the diffusivity and the squared temperature gradients are relatively small (Figs. 9c,e,g; compare dashed and dash-dotted lines),

$$\kappa_{\text{Taylor}} \equiv \frac{\overline{\kappa |\nabla T|^2}}{|\nabla T|^2} \approx \overline{\kappa},$$
(14)

i.e., squeeze dispersion only slightly modulates bulk tracer spreading (Wagner et al. 2019). This contribution to diapycnal spreading from the tracer-weighted diffusivity remains roughly constant in time, aside from an initial transient as the bulk of the tracer spreads toward shallower topographic features and therefore experiences more vigorous mixing on average (Figs. 7b and 9c,e,g). The substantial temporal variability in the diapycnal spreading experienced by the tracers is instead driven by leading-order diapycnal distortion effects (Figs. 9d–g). Depending on the instantaneous distribution of the tracer in space, this term can vary substantially both in magnitude and sign, either amplifying the tracer-weighted diffusivity by up to 75% or neutralizing it entirely (Fig. 9g; at 40 and 400 days, respectively).

d. Untangling diapycnal distortion due to stretching and contraction effects

Motivated by the dipole example in section 2b, we aim to gain a deeper understanding of these diapycnal distortion

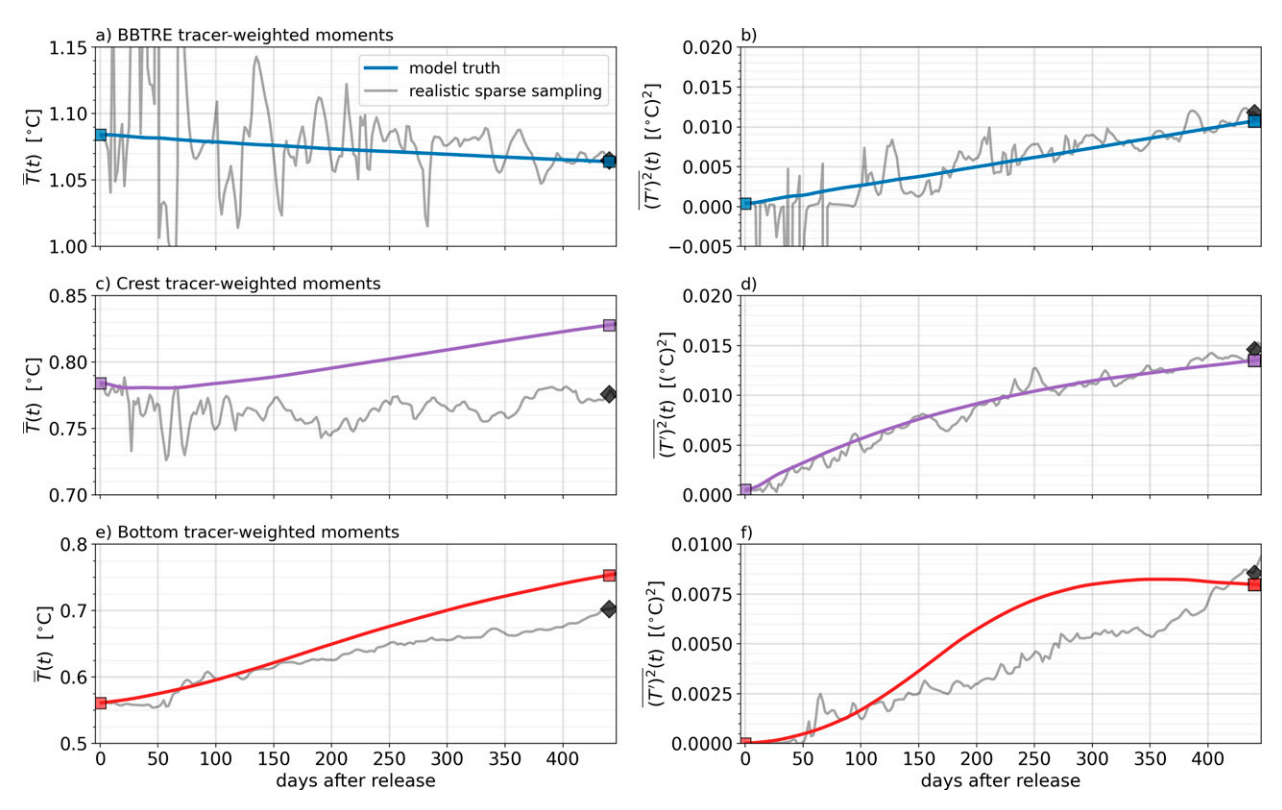


FIG. 12. Evolution of the first and (centered) second tracer-weighted temperature moments, exactly diagnosed from the full solution (colored lines) and estimated from a sparse subsampling (gray lines)—see sampling stations in Figs. 5a and 5b. Squares denote the moments at days 0 and 440. Diamonds denote subsampled estimates of the moments at day 440, which can be combined with a priori knowledge of the tracer at day 0 to estimate Eqs. (16) and (17).

effects by decomposing the distortion term κ_{ω} in (ω, T) space (Fig. 10, as in Fig. 1b), i.e., by decomposing the volume integral into a sum over subvolumes:

$$\frac{\kappa_{\omega}}{\kappa_{\text{Taylor}}} = \sum_{i,j} \int_{\mathcal{V}_{\{\omega_i\} \cap \{T_j\}}} \frac{2\omega' T' c}{\mathcal{M} |\overline{\nabla T}|^2} \kappa_{\text{Taylor}} dV, \tag{15}$$

where $\mathcal{M} \equiv \int_{\mathcal{V}} c \, dV$ is the total tracer mass and the intersection of subsets $\{\omega_i\}$ and $\{T_i\}$ correspond to distinct subvolumes $\mathcal{V}_{\{\omega\}\cap\{T\}}$ of the tracer distribution, defined by their (ω, T) characteristics. In (15) and throughout this section, we normalize by the total effective diapycnal diffusion κ_{Taylor} to quantify the relative importance of the unconventional distortion effects compared to the more conventional diapycnal (or vertical) diffusion (Taylor 1922); for example, $\kappa_{\omega}/\kappa_{\text{Taylor}} = 100\%$ implies stretching doubles the diffusive spreading rate while $\kappa_{\omega}/\kappa_{\rm Taylor} = -100\%$ implies net contraction is sufficiently strong to exactly offset the diffusive contribution to spreading. Figure 10 shows heat maps of the contributions from relatively narrow (ω', T') bins as well as the summed contributions from each of the quadrants delineated by the respective signs of ω' and T'. Figure 11 shows PDFs of tracer mass in (ω, T) space; by comparing with Fig. 10, we attribute most of the diapycnal distortion to the small amounts of strongly anomalous tracer, i.e., with large $|\omega'|$ and |T'|.

We begin by exploring why the BBTRE tracer experiences very little net diapycnal distortion despite being stretched by strongly bottom-enhanced mixing (Ruan and Ferrari 2021). At day 100 (Fig. 10a), we find the tracer is diapycnally stretched $(\omega' T' > 0)$ by an additional 23% κ_{Taylor} (hereafter dropping the κ_{Taylor} for convenience) as relatively cold tracer relatively downwells (T' < 0, $\omega' < 0$; increasing spreading by 16%) and relatively warm tracer relatively upwells $(T' > 0, \omega' > 0;$ increasing spreading by 7%). However, a very small amount of cold tracer has made it close enough to the seafloor to be entrained in the BBL, where it upwells sufficiently vigorously to result in a contraction effect of -9% which, supplemented by an additional -2% contraction from warm downwelling tracer, results in a reduction of the net diapycnal stretching to only 23% - 11% = 12%. By day 440 (Fig. 10b), this cold patch of tracer is pulled further toward the bottom and its stretching effect grows to 69%, but is offset by an even larger diapycnal contraction of -76% in the BBL; combined with a net stretching of only 11% - 10% = 1% from the warm tracer, diapycnal distortion has a negligible net contraction effect of -6%.

At the other extreme, we aim to understand how the Bottom tracer undergoes first a large net diapycnal stretching effect and then an even larger net diapycnal contraction effect later on in its evolution. Over the first 100 days, most of the tracer upwells in the BBL and warms (Fig. 6f). Some of the warmest tracer

remains in the BBL, where its upwelling drives a substantial diapycnal stretching of 91% (Fig. 10c). However, part of this warm branch of the tracer is entrained into the SML, where its downwelling drives a largely compensating diapycnal contraction effect of -80%. The relatively cold patch of tracer that is left behind contributes a stretching of 42% - 15% = 27%, dominated by its relatively slow upwelling ($\omega > 0$ but $\omega' < 0$), bringing the net diapycnal stretching to 91% - 80% + 27% = 38%. By day 440, however, both the warm and cold branches of the tracer distribution (Fig. 51) drive large diapycnal contraction effects: -98% due to cold upwelling upstream of the sill and -101% due to warm downwelling downstream of the sill (Figs. 5j,l and 10d). Diapycnal stretching of 93% from the other quadrants offset about half of this diapycnal contraction, but the net diapycnal contraction of -106% still overwhelms the spreading due to the in situ diffusivity, causing the Bottom tracer to temporarily contract in temperature space—contradicting conventional intuition about the bulk effects of downgradient diapycnal diffusion!

e. Relevance to realistically sparse tracer surveys

The above results benefit from the luxury of knowing the exact tracer distributions $c(\mathbf{x}, t)$ and temperature fields $T(\mathbf{x}, t)$, as well as their instantaneous tendencies, everywhere and at all times; in practice, shipboard sampling strategies provide snapshots of c and T which are extremely sparse in both space and time.

Integrating the moment equations [Eqs. (3) and (4)] between two surveys at t_i and $t_j = t_i + \Delta t$ yields more useful forms that at least do not depend on intractable time derivatives:

$$\frac{\overline{T}(t_j) - \overline{T}(t_i)}{\Delta t} = 2\langle \overline{\omega} \rangle \quad \text{and}$$
 (16)

$$\frac{1}{2} \frac{\overline{(T')^2}(t_j) - \overline{(T')^2}(t_i)}{\Delta t} = \langle \overline{\kappa} | \overline{\nabla} T |^2 + 2 \overline{\omega'} T' \rangle, \tag{17}$$

where $\langle \, \star \, \rangle \equiv (1/\Delta t) \int_{t_i}^{t_i} \star dt$ denotes the time mean. Tracers are typically injected along a chosen buoyancy surface, i.e., the initial conditions $\overline{T}(t_0) = T_0$ and $(T')^2(t_0) \simeq 0$ are known a priori by design, allowing the moments to be estimated from a single survey at some time $t_j = \underline{t_0} + \Delta t$ after release. Figure 12 shows time series of $\overline{T}(t)$ and $(T')^2(t)$ for all three simulated tracer releases, from which the moments are readily calculated.

In practice, since the time between consecutive tracer surveys is typically much longer than their durations, a reasonable first approximation is to treat each observational survey as a snapshot in time, e.g., at the cruise's midpoint. Motivated by the BBTRE, in which the first major survey started roughly 14 months after release, we use (16) and (17) to *exactly* diagnose the time-mean moments (Figs. 6b,d,f and 9b,d,f, colored squares) based only on a single instantaneous snapshot of the temperature and tracer fields 440 days (14.5 months) after release (Fig. 12, colored squares).

Although temporal sparsity in sampling can be conveniently addressed in this way by integration, spatial sparsity requires a different approach. Motivated by the $\mathcal{O}(60)$ km spacing of the BBTRE sampling strategy (Fig. 2a, red dots),

we generate synthetic tracer and buoyancy profiles by subsampling our simulation every 60 km along the thalweg of the canyon (Figs. 5a,b, red dots). One approach to making sense of these sparse data employs inverse methods, such as objective mapping, to estimate snapshots of the full three-dimensional tracer and buoyancy fields for each survey (as in Ledwell et al. 2000). Here, we take the much simpler approach of approximating the full three-dimensional tracer-weighted volume averages with tracer-weighted sample averages,

$$\frac{\int_{\mathcal{V}} c\phi \ dV}{\int_{\mathcal{V}} c\phi \ dV} \simeq \frac{\sum_{n,k} c(x_n, y_n, z_k)\phi(x_n, y_n, z_k)\Delta z(k)}{\sum_{n,k} c(x_n, y_n, z_k)\Delta z(k)},$$
(18)

where subscript n and k denote the synthetic cast numbers and vertical levels, respectively, and $\Delta z(k)$ is the vertical resolution of the observations. This sample-averaging approach, which effectively ignores any horizontal covariance information, is similar in spirit to that used in many TRE analyses (e.g., Ledwell and Watson 1991; Ledwell et al. 1998; Holtermann et al. 2012; Watson et al. 2013). Despite this rather dramatic subsampling of our rich numerical solution, the tracer-weighted sample-averaged estimates (18) generally yield estimates within 20% of the true time-mean (Fig. 12; compare black diamonds to colored squares). The one exception is the Crest tracer's first moment, for which the sample-averaged estimate suggests the tracer is slowly downwelling when it is in fact upwelling (Fig. 12c); the Crest tracer's displacement is prone to large relative errors because it is the small residual of large upwelling and downwelling components.

By generating synthetic observations for all times between the tracer release and 440 days, we explore how the accuracy of the sampling strategy depends on the horizontal scales of the tracer distributions (Fig. 12, gray lines). Estimates are likely to be error-prone until the initially narrow tracer distri-

butions [with widths $\sqrt{(x')^2} = \sigma_x = 3.5$ km] have spread over horizontal distances comparable to the 60 km spacing of sampling stations. For example, estimates of the BBTRE moments are initially extremely noisy and only begin to stabilize

when they reach a width of $\sqrt{(x')^2} \approx 20\,\mathrm{km}$ after about 200 days after release (Figs. 12a,b). By contrast, the estimates for the Crest and Bottom release are much more stable (Figs. 12c–f), presumably because the blocking of cross-canyon flow by the canyon sidewalls forces the tracer to homogenize more rapidly across the canyon, reducing the errors due to undersampling in the cross-canyon direction (see Fig. 5). Interestingly, while the sample-averaged estimate of the Bottom tracer's spreading after 440 days is reasonably accurate, earlier surveys would have completely missed the nonmonotonic time dependence caused by the leading-order diapycnal distortion effects (Fig. 12f).

5. Discussion and conclusions

By applying Ruan and Ferrari's (2021) buoyancy moment diagnostics to our quasi-realistic regional simulation of mixing-driven abyssal flows (described in detail in Drake et al. 2022), we confirm the qualitative results of Holmes et al.'s (2019) idealized

analysis of the BBTRE release in the SML: over time, boundary suppression in the BBL almost exactly compensates for vertical stretching in the SML, such that the net diapycnal spreading of the BBTRE tracer coincidentally provides a reasonably accurate estimate (within 10%) of the tracer-weighted in situ diffusivity (Fig. 9c, compare black diamond with blue circle). These simulation results are supported by a recent reanalysis of the BBTRE observations, which reveal a similarly negligible diapycnal distortion effect of $<10\%\kappa_{\rm Taylor}$ (Fig. 9b; J. R. Ledwell 2022, unpublished manuscript).

Quantitatively, however, the diapycnal spreading we simulate for the BBTRE tracer is smaller than the observed spreading by roughly a factor of 2 (Fig. 9c), suggesting either the microstructure measurements we use to tune the prescribed diffusivity profile are biased low or our simulation is missing other unknown tracer dispersion processes. This is roughly consistent with J. R. Ledwell's (2022, unpublished manuscript) inversion of a 1D advection-diffusion model, which produced optimal diffusivities about twice as large as the microstructure's sample mean. Our results are also consistent with the conclusion of the companion manuscript (Drake et al. 2022), which shows that biases in the simulated flows and stratification of the BBTRE fracture zone canyon also suggest the imposed microstructure mixing rates may be biased low by a factor of roughly 2. These BBTRE-specific results are consistent with the broader observational literature, which unanimously finds that mixing rates estimated from TREs are larger than those suggested by collocated microstructure measurements (Ruan and Ferrari 2021).

In contrast to the BBTRE release, we find that for nearbottom tracers, diapycnal distortion can be of either sign (depending on the tracer distribution) and of comparable magnitude to the tracer-weighted in situ diffusivity, $|\kappa_{\omega}| \sim \kappa_{\text{Taylor}} \simeq \overline{\kappa}$ (Fig. 9g). Our simulations demonstrate that three-dimensional eddies and topographic effects have a leading-order impact on diapycnal tracer spreading, as tracer distributions are chaotically transported in and out of regions of vigorous mixing. Unsurprisingly, diapycnal stretching and contraction effects are much stronger—and more variable—in our three-dimensional flows over rough topography than the already substantial effects reported by Holmes et al. (2019) for one-dimensional boundary layers with parameterized isopycnal eddy stirring. In all of Holmes et al.'s (2019) near-bottom releases, diapycnal contraction reduces spreading rates by a factor of 2-3, which even in the case of vigorous isopycnal stirring only slightly deviates from predicted factor of $[1 - (2/\pi)]^{-1} \approx 2.8$ for the long-time limit of 1D diffusion on the half-line. By contrast, for our Bottom tracer release, diapycnal distortion amplifies diapycnal spreading by a stretching of $\mathcal{O}(75)\% \kappa_{\text{Taylor}}$ in the first few dozen days of the simulation and later suppresses diapycnal spreading by a contraction of $\mathcal{O}(-100)\%\kappa_{\text{Taylor}}$ for the last few dozen days (Figs. 9g and 7c)!

Given that rough topography generally implies strong bottomenhanced diapycnal mixing (Polzin et al. 1997; Waterhouse et al. 2014), which is in turn thought to incite bottom mixed layer eddies (Callies 2018; Wenegrat et al. 2018; Ruan and Callies 2020), significant diapycnal stretching and contraction effects are to be expected near sloping rough topography in the abyss, such as along the global midocean ridge system (Ledwell et al. 2000; Thurnherr et al. 2005, 2020) and within continental slope canyons (Nazarian et al. 2021; Hamann et al. 2021; Alberty et al. 2017). In these regions, unlike for interior ocean releases such as BBTRE, tracer-based estimates of mixing rates must take into account the three-dimensional history of the tracer distribution's evolution.

It has long been appreciated that the interpretation of tracer spreading near topography requires greater care because of enhanced boundary mixing and hypsometric effects (e.g., Ledwell and Hickey 1995). Attempts to modify the conventional 1D model to include these boundary effects are varied: e.g., by separately modeling the tracer distribution in "boundary" and "interior" regions (Ledwell and Hickey 1995; Holtermann et al. 2012; Ledwell et al. 2016), by allowing vertical structure in the diffusivity and hypsometry in 1D advectiondiffusion models (Ledwell et al. 2000; Holtermann et al. 2012), or by extending the 1D model to a 2D (Watson et al. 2013) or 3D (Mackay et al. 2018) model to account for lateral transport into and out of regions of strong mixing. However, the ad hoc derivations of these models render them difficult to interpret and compare, suggesting a complementary role for the more exact buoyancy moment approach (Holmes et al. 2019; Ruan and Ferrari 2021).

Mesoscale/submesoscale-resolving regional simulations of TREs are now feasible thanks to exponential increases in computational power (Tulloch et al. 2014; Mashayek et al. 2017; K. Ogden et al. 2022, unpublished manuscript; this study) and have been used a posteriori to help interpret observations and explain differences between mixing rates inferred from TREs and microstructure profiles. However, such simulations have not yet been used to evaluate (or improve upon) operational methods for comparing tracer and microstructure observations, such as by using a "perfect model" framework in which simulated tracer observations are inverted in an attempt to recover the prescribed "true" diffusivity field. As an illustrative example, in section 4e, we attempt to estimate in situ diffusivities by applying the exact buoyancy moment approach to realistically sparse synthetic observational campaigns. The results suggest that diapycnal distortion effects, which are poorly represented within conventional inverse models, result in $\mathcal{O}(1)$ structural errors in estimates of the tracer-weighted in situ diffusivity $\overline{\kappa}$. Sampling errors are relatively small (<20%) by comparison and are likely overestimated here because our BBTRE simulation underestimates the observed isopycnal spreading rate (and thus the effective horizontal sampling resolution) by roughly a factor of 5 (Ledwell et al. 2000) due to the exclusion of externally forced currents and mesoscale stirring in our narrow simulation domain.

In the future, a priori or real-time numerical simulations could be used to inform TRE sampling strategies—current best practice is to roughly estimate horizontal transport from real-time velocity estimates from ADCPs or altimetry (M.-J. Messias and J. R. Ledwell 2021, personal communication). To our knowledge, this has not yet been done, with the notable exception of the "Bottom Boundary Layer Turbulence and Abyssal Recipes" team (BLT; NSF Award 1756251), who used TRE simulations to inform the experiment's planning and sampling strategies.

While our results suggest that estimates of in situ diffusivity profiles from observations of a tracer's second buoyancy moment may be corrupted by complicated diapycnal distortion processes (Fig. 7c; consistent with Holmes et al. 2019), they also support Holmes et al.'s (2019) hypothesis that the first buoyancy moment provides a more robust and straightforward estimate of the in situ turbulent buoyancy flux convergence (or buoyancy velocity ω ; Fig. 7a). However, even the first-moment diagnostics can be misleading convolutions of opposing upwelling and downwelling components (Fig. 8), making them challenging to interpret and prone to significant sampling errors (Fig. 12c). Nevertheless, as long as a sizable fraction of the tracer (here $\gg \overline{W}_{\rm SML}^T/\overline{W}_{\rm BBL}^{T} \approx 10\%$; Fig. 8) remains in the BBL and the sampling resolution is sufficiently high, the change in the first buoyancy moment is likely to provide at least a reasonable lower-bound estimate of the average in situ upwelling in the BBL (section 2b). This is a promising result in light of the ongoing BLT TRE, which aims to provide the first in situ estimates of BBL upwelling. Shortterm surveys, when the tracer distribution is still relatively compact (e.g., from a dye release experiment), may be interpreted as lower-bound estimates of BBL upwelling; on the other hand, long-term surveys, when the tracer roughly equally occupies the BBL and SML, may be interpreted as estimates of net upwelling. Combined, these two estimates could constrain the strength of the amplification factor (the ratio of strictly upwelling transport in the BBL to net upwelling), which is predicted by theory to be much larger than 1 but remains poorly understood (Ferrari et al. 2016; McDougall and Ferrari 2017; Callies 2018; Holmes and McDougall 2020). In combination with previous observations of tracer-weighted diapycnal sinking in the SML above rough topography (Ledwell et al. 2000), observations of vigorous tracer-weighted diapycnal upwelling in the BBL would be compelling direct evidence for the emerging paradigm of bottom mixing layer control of the abyssal meridional overturning circulation (Ferrari et al. 2016; de Lavergne et al. 2016a; Callies 2018; Callies and Ferrari 2018; Drake et al. 2020, 2022).

Acknowledgments. We thank Jim Ledwell for countless insightful discussions about this work and comments on previous versions of the manuscript. We also thank Ryan Holmes and an anonymous reviewer for suggestions that improved the manuscript. We thank the crews of the BBTRE and DoMORE field campaigns for collecting the observations that motivated this work. We acknowledge funding support from National Science Foundation Awards 1536515 and 1736109. This material is based upon work supported by the National Science Foundation Graduate Research Fellowship Program under Grant 174530. Any opinions, findings, and conclusions or recommendations expressed in this material are those of the author(s) and do not necessarily reflect the views of the National Science Foundation. This research is also supported by the NOAA Climate and Global Change Postdoctoral Fellowship Program, administered by UCAR's Cooperative Programs for the Advancement of Earth System Science (CPAESS) under Award NA18NWS4620043B.

Data availability statement. The source code for the MITgcm simulations and all of the Python code necessary to produce the figures is publicly available at github.com/hdrake/simbbtre. Our analysis of labeled data arrays is greatly simplified by the xarray package in Python (Hoyer and Hamman 2017).

APPENDIX A

A Slope-Native MITgcm Configuration of Bottom Mixing Layer Flows in the Brazil Basin

We use a hydrostatic formulation of the MIT General Circulation Model (MITgcm; Marshall et al. 1997) to simulate mixing-driven flows in the BBTRE canyon and the transient evolution of three localized tracer releases. Regional bathymetry is extracted from the Global Bathymetry and Topography at 15 Arc Sec dataset (SRTM15+; Tozer et al. 2019) and interpolated onto a locally tangent Cartesian grid $(\hat{x}, \hat{y}, \hat{z})$ aligned with the BBTRE canyon, where \hat{x} denotes the along-canyon (or cross-ridge) dimension, \hat{y} denotes the cross-canyon (or along-ridge) dimension, and $\hat{d}(\hat{x}, \hat{y})$ is the seafloor depth (Fig. 2a). The domain includes both the BBTRE tracer release location and ample room for up-canyon advection of the tracer, which is anticipated based on both the BBTRE observations (Ledwell et al. 2000) and bottom boundary layer theory (Holmes et al. 2019).

Inspired by 1D boundary layer theory and the idealized 3D simulations of Callies (2018), we configure a slope-native implementation of the MITgcm (only summarized here; details in Drake et al. 2022). First, we separate a quiescent $(\mathbf{u}_b \equiv \mathbf{0})$ background with uniform stratification $\Lambda \equiv dT_b/d\hat{z} = 9 \times 10^{-4} \, ^{\circ}\text{C m}^{-1}$ from the solution and solve only for the perturbations $T_p \equiv T - T_b$ and $\mathbf{u}_n \equiv \mathbf{u}$ about this background state, which requires adding the appropriate tendency terms to the perturbation temperature and momentum equations, respectively. Second, we transform the MITgcm into the coordinates of the mean slope, with slope angle $\theta = 1.26 \times 10^{-3}$ (Fig. 2b), allowing us to apply periodic boundary conditions to the perturbations T_p and \mathbf{u}_p (and the released tracer concentration c) in the (x, y) plane of the mean slope. The detrended seafloor depth is given by $d(x,y) \equiv \hat{d}(\hat{x},\hat{y}) - \hat{x} \tan \theta$. Mean cross-slope (along-canyon) upwelling and downwelling across the periodic x boundary provide infinite sources of dense and light waters, respectively, allowing equilibration of the solution without requiring an explicit restoring force to balance the homogenizing tendency of turbulent mixing (Garrett 1991).

A companion paper (Drake et al. 2022) explores the mixing-driven circulations that arise in this simulation in detail. Bottom-enhanced mixing spins up a broad diapycnal sinking in the well-stratified interior and a vigorous diabatic upwelling in the bottom boundary layer. Despite a modest restratifying effect by this mean overturning circulation, the solution develops a substantial horizontal temperature gradient which stores available potential energy. This available potential energy fuels instabilities, which grow to finite amplitude and are characterized by a Rossby number of Ro \approx 1, i.e., are submesoscale in nature (see, e.g., McWilliams 2016). One effect of these eddies is to restratify the bottom 20 m or so, bringing the simulated

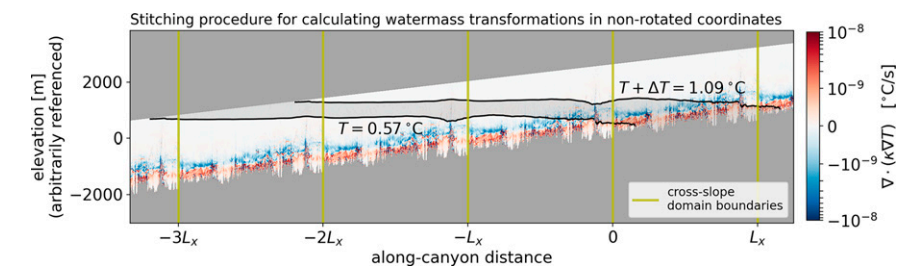


FIG. B1. Turbulent buoyancy (temperature) flux convergence along the trough of the BBTRE canyon. Vertical olive lines show along-canyon boundaries of the simulation domain; the solution is doubly periodic in buoyancy perturbations, but discontinuous in the total buoyancy in the along-canyon direction due to a constant background mean slope and stratification. For the small mean slopes considered here, computing water-mass transformations thus requires reconstructing the full extent of buoyancy surfaces by stitching together multiple copies of the domain, each translated by a multiple of the domain extent L_x and by a background temperature jump $\Delta T = \Lambda \Delta z \approx 0.52^{\circ}\text{C}$ (where $\Delta z = L_x \tan \theta$ is the layer thickness).

stratification more in line with observations than 1D boundary layer dynamics would suggest (Callies 2018; Ruan and Callies 2020). A hierarchy of progressively simplified versions of the simulation are used as mechanism denial experiments to show the importance of topographic blocking and steering in controlling the near-bottom stratification, which in turn controls the magnitude of near-bottom diapycnal upwelling.

In our slope-native configuration, one should imagine infinitely many copies of the TRE, each separated by a horizontal distance $L_x = 480$ km (domain length) and vertical height $L_x \tan \theta \approx 1000$ m [corresponding to a background temperature difference $\Delta T \approx (dT_b/d\hat{z})L_x \sin\theta = 0.52$ °C]. A limitation of this configuration is that when tracer crosses the \mathbf{x} boundary, it experiences an unphysical jump in temperature of ΔT . This problem can be significantly delayed, but not avoided entirely, by recentering the domain around the tracer blobs before adding the constantly stratified background temperature field T_b back in (e.g., see Fig. 5). By 1000 days, however, enough of the tracer has crossed the periodic x boundaries that the copies of the tracers begin significantly interfering with each other and the temperature moment calculations become meaningless. This does not affect the results presented here since we truncate the simulations after the timing of the first BBTRE survey (14 months \approx 440 days), well before these issues arise. For all of the analysis presented here, we crop the infinitely repeating domain to include only a single copy of the tracer distribution (similar to the approach used to compute water-mass transformations in appendix B).

APPENDIX B

Eulerian and Tracer-Weighted Water-Mass Transformations

A natural framework for understanding the drivers of diapycnal transport is water-mass transformation analysis (Walin 1982; Marshall et al. 1999), which reframes the buoyancy budget in buoyancy space by integrating along buoyancy surfaces (or over buoyancy classes). Following

Ferrari et al. (2016), the diapycnal transport $\mathcal{E}(T,t)$ across a buoyancy surface $\mathcal{A}(T)$ is given by

$$\mathcal{E}(T,t) \equiv \iint_{A(T)} \mathbf{e} \cdot \mathbf{n} \ dA = \partial_T \int_{\mathcal{V}(\tilde{T} < T)} \omega dV, \tag{B1}$$

where $\mathbf{e} \equiv [\mathbf{u} \cdot \mathbf{n} - (T_t/|\nabla T|)]\mathbf{n}$ is the diapycnal velocity and $\mathcal{V}(\tilde{T} < T)$ is the volume enclosing any water denser than T. Since our simulations have not fully equilibrated in the SML, diapycnal transports include two components: flow across a buoyancy surface and the movement of the buoyancy surfaces themselves. In the present context, it is useful to distinguish contributions to the diapycnal transport from a strictly upwelling BBL component, where the integral is only evaluated over the strictly upwelling volume $\mathcal{V}(\tilde{T} < T; \omega > 0)$, and a strictly downwelling SML component, similarly defined (see Fig. B1).

In practice, meaningful evaluation of this integral in the slope-native configuration requires stitching together $H/(L_x \tan \theta) \approx \mathcal{O}(5)$ periodic copies of the domain (where H is the height of the domain) before adding in the background buoyancy field B, so that each isopycnal can be followed all the way from where it intersects with the seafloor to the interior far-field where mixing is weak (Fig. B1). Further, because our simulation is periodic in the cross-slope (along-canyon) direction \mathbf{x} (and thus in mean buoyancy), the resulting watermass transformations are periodic over a buoyancy interval $\Delta T = \Lambda L_x \tan \theta \approx 0.52^{\circ}\mathrm{C}$. Temporal variability of water-mass transformations is small relative to the other variations we focus on, so all results hereafter refer to their time-mean.

Averaging over a buoyancy layer of thickness ΔT yields a single representative value of the net water-mass transformation,

$$\overline{\mathcal{E}}^T \equiv \frac{1}{\Delta T} \int_{T}^{T+\Delta T} \mathcal{E}(\tilde{T}) \ d\tilde{T} = \int_{\mathcal{V}(T < \tilde{T} < T+\Delta T)} \frac{\omega}{\Delta T} \ dV. \tag{B2}$$

This equation is also reminiscent of that for the evolution of the first tracer-weighted buoyancy moment (5), with the whole domain being weighted equally as opposed to being weighted by the tracer concentration.

The detailed height-above-bottom (η , for short) structure of upwelling and downwelling water-mass transformations are also of interest, since these are more directly comparable with measurements from vertical profilers, 1D BBL theory, and the diapycnal transport of localized tracers. Building upon Holmes and McDougall (2020), we define the height-above-bottom cumulative water-mass transformation as

$$\overline{\mathcal{E}}^{T}(\eta) = \int_{\mathcal{V}(T_0 < \tilde{T} < T_0 + \Delta T; \tilde{\eta} < \eta)} \frac{\omega}{\Delta T} \, dV. \tag{B3}$$

We aim to convert these water-mass transformations into effective vertical velocities, for more direct comparison with the tracer diagnostics. Loosely, taking the slope-normal (or η) derivative provides the up-slope upwelling flux (in m² s⁻¹) at a given height above bottom:

$$\frac{\partial}{\partial \eta} \overline{\mathcal{E}}^T(\eta) = \frac{\partial}{\partial \eta} \int_{\mathcal{V}(T_0 < \tilde{T} < T_0 + \Delta T; \tilde{\eta} < \eta)} \frac{\omega}{\Delta T} \, dV. \tag{B4}$$

Multiplying by $\sin \theta$ approximately converts this to a vertical flux, and dividing by the width L_y of the domain finishes the conversion to the effective velocity (B5),

$$\overline{W}^{T}(\eta) \equiv \frac{\sin \theta}{L_{y}} \frac{\partial}{\partial \eta} \overline{\mathcal{E}}^{T}(\eta). \tag{B5}$$

Profiles of $\overline{W}^T(\eta)$ are shown in Fig. 8 and, after convolution with idealized height-above-bottom tracer distributions, compare favorably with the diagnosed vertical structure of tracer upwelling.

REFERENCES

- Abernathey, R. P., I. Cerovecki, P. R. Holland, E. Newsom, M. Mazloff, and L. D. Talley, 2016: Water-mass transformation by sea ice in the upper branch of the Southern Ocean overturning. *Nat. Geosci.*, 9, 596–601, https://doi.org/10.1038/ ngeo2749.
- Alberty, M. S., S. Billheimer, M. M. Hamann, C. Y. Ou, V. Tamsitt, A. J. Lucas, and M. H. Alford, 2017: A reflecting, steepening, and breaking internal tide in a submarine canyon. *J. Geophys. Res. Oceans*, 122, 6872–6882, https://doi.org/10. 1002/2016JC012583.
- Baker, M. A., and C. H. Gibson, 1987: Sampling turbulence in the stratified ocean: Statistical consequences of strong intermittency. *J. Phys. Oceanogr.*, 17, 1817–1836, https://doi.org/10. 1175/1520-0485(1987)017<1817:STITSO>2.0.CO;2.
- Bryan, K., and L. J. Lewis, 1979: A water mass model of the world ocean. J. Geophys. Res., 84, 2503–2517, https://doi.org/ 10.1029/JC084iC05p02503.
- Cael, B. B., and A. Mashayek, 2021: Log-skew-normality of ocean turbulence. *Phys. Rev. Lett.*, **126**, 224502, https://doi.org/10. 1103/PhysRevLett.126.224502.
- Callies, J., 2018: Restratification of abyssal mixing layers by sub-mesoscale baroclinic eddies. J. Phys. Oceanogr., 48, 1995–2010, https://doi.org/10.1175/JPO-D-18-0082.1.
- —, and R. Ferrari, 2018: Dynamics of an abyssal circulation driven by bottom-intensified mixing on slopes. *J. Phys. Ocean*ogr., 48, 1257–1282, https://doi.org/10.1175/JPO-D-17-0125.1.

- Clément, L., A. M. Thurnherr, and L. C. St. Laurent, 2017: Turbulent mixing in a deep fracture zone on the Mid-Atlantic Ridge. J. Phys. Oceanogr., 47, 1873–1896, https://doi.org/10.1175/JPO-D-16-0264.1.
- de Lavergne, C., G. Madec, J. Le Sommer, A. J. G. Nurser, and A. C. Naveira Garabato, 2016a: The impact of a variable mixing efficiency on the abyssal overturning. *J. Phys. Oceanogr.*, 46, 663–681, https://doi.org/10.1175/JPO-D-14-0259.1.
- —, —, —, and —, 2016b: On the consumption of Antarctic Bottom Water in the abyssal ocean. *J. Phys. Oceanogr.*, **46**, 635–661, https://doi.org/10.1175/JPO-D-14-0201.1.
- —, and Coauthors, 2020: A parameterization of local and remote tidal mixing. J. Adv. Model. Earth Syst., 12, e2020MS002065, https://doi.org/10.1029/2020MS002065.
- Dematteis, G., and Y. V. Lvov, 2021: Downscale energy fluxes in scale-invariant oceanic internal wave turbulence. *J. Fluid Mech.*, 915, A129, https://doi.org/10.1017/jfm.2021.99.
- De Szoeke, R. A., and A. F. Bennett, 1993: Microstructure fluxes across density surfaces. *J. Phys. Oceanogr.*, **23**, 2254–2264, https://doi.org/10.1175/1520-0485(1993)023<2254:MFADS>2. 0.CO;2.
- Dillon, T. M., 1982: Vertical overturns: A comparison of Thorpe and Ozmidov length scales. J. Geophys. Res., 87, 9601–9613, https://doi.org/10.1029/JC087iC12p09601.
- Drake, H. F., 2021: Control of the abyssal ocean overturning circulation by mixing-driven bottom boundary layers. Ph.D. thesis, Massachusetts Institute of Technology, 157 pp., https:// doi.org/10.1575/1912/27424.
- —, R. Ferrari, and J. Callies, 2020: Abyssal circulation driven by near-boundary mixing: Water mass transformations and interior stratification. *J. Phys. Oceanogr.*, **50**, 2203–2226, https://doi.org/10.1175/JPO-D-19-0313.1.
- ——, X. Ruan, J. Callies, K. Ogden, A. M. Thurnherr, and R. Ferrari, 2022: Dynamics of eddying abyssal mixing layers over rough topography. *J. Phys. Oceanogr.*, 3199–3219, https://doi.org/10.1175/JPO-D-22-0009.1.
- Ferrari, R., A. Mashayek, T. J. McDougall, M. Nikurashin, and J.-M. Campin, 2016: Turning ocean mixing upside down. J. Phys. Oceanogr., 46, 2239–2261, https://doi.org/10.1175/ JPO-D-15-0244.1.
- Garrett, C., 1991: Marginal mixing theories. *Atmos.–Ocean*, **29**, 313–339, https://doi.org/10.1080/07055900.1991.9649407.
- ——, and W. Munk, 1972: Space-time scales of internal waves. Geophys. Astrophys. Fluid Dyn., 3, 225–264, https://doi.org/ 10.1080/03091927208236082.
- —, and —, 1975: Space-time scales of internal waves: A progress report. J. Geophys. Res., 80, 291–297, https://doi.org/10.1029/JC080i003p00291.
- —, P. MacCready, and P. Rhines, 1993: Boundary mixing and arrested Ekman Layers: Rotating stratified flow near a sloping boundary. *Annu. Rev. Fluid Mech.*, 25, 291–323, https:// doi.org/10.1146/annurey.fl.25.010193.001451.
- Gregg, M. C., 1989: Scaling turbulent dissipation in the thermocline. J. Geophys. Res., 94, 9686–9698, https://doi.org/10.1029/ JC094iC07p09686.
- —, T. B. Sanford, and D. P. Winkel, 2003: Reduced mixing from the breaking of internal waves in equatorial waters. *Nature*, **422**, 513–515, https://doi.org/10.1038/nature01507.
- —, E. A. D'Asaro, J. J. Riley, and E. Kunze, 2018: Mixing efficiency in the ocean. *Annu. Rev. Mar. Sci.*, 10, 443–473, https://doi.org/10.1146/annurev-marine-121916-063643.
- Hamann, M. M., M. H. Alford, A. J. Lucas, A. F. Waterhouse, and G. Voet, 2021: Turbulence driven by reflected internal

- tides in a supercritical submarine canyon. *J. Phys. Oceanogr.*, **51**, 591–609, https://doi.org/10.1175/JPO-D-20-0123.1.
- Henyey, F. S., J. Wright, and S. M. Flatté, 1986: Energy and action flow through the internal wave field: An eikonal approach. J. Geophys. Res., 91, 8487–8495, https://doi.org/10.1029/JC091iC07p08487.
- Hogg, N., P. E. Biscaye, W. D. Gardner, and W. J. Schmitz Jr., 1982: On the transport and modification of Antarctic bottom water in the Vema Channel. J. Mar. Res., 40, 231–263.
- Holmes, R. M., and T. J. McDougall, 2020: Diapycnal transport near a sloping bottom boundary. *J. Phys. Oceanogr.*, **50**, 3253–3266, https://doi.org/10.1175/JPO-D-20-0066.1.
- —, C. de Lavergne, and T. J. McDougall, 2019: Tracer transport within abyssal mixing layers. *J. Phys. Oceanogr.*, 49, 2669–2695, https://doi.org/10.1175/JPO-D-19-0006.1.
- Holtermann, P. L., L. Umlauf, T. Tanhua, O. Schmale, G. Rehder, and J. J. Waniek, 2012: The Baltic sea tracer release experiment: 1. Mixing rates. J. Geophys. Res., 117, C01021, https://doi.org/10.1029/2011JC007439.
- Hoyer, S., and J. Hamman, 2017: Xarray: N-D labeled arrays and datasets in Python. J. Open Res. Software, 5, 10, https://doi. org/10.5334/jors.148.
- Huang, R. X., and X. Jin, 2002: Deep circulation in the South Atlantic induced by bottom-intensified mixing over the midocean ridge. *J. Phys. Oceanogr.*, 32, 1150–1164, https://doi.org/ 10.1175/1520-0485(2002)032<1150:DCITSA>2.0.CO;2.
- Kunze, E., E. Firing, J. M. Hummon, T. K. Chereskin, and A. M. Thurnherr, 2006: Global abyssal mixing inferred from lowered ADCP shear and CTD strain profiles. *J. Phys. Oceanogr.*, 36, 1553–1576, https://doi.org/10.1175/JPO2926.1.
- Ledwell, J. R., and A. J. Watson, 1991: The Santa Monica basin tracer experiment: A study of diapycnal and isopycnal mixing. J. Geophys. Res., 96, 8695–8718, https://doi.org/10.1029/ 91JC00102.
- —, and B. M. Hickey, 1995: Evidence for enhanced boundary mixing in the Santa Monica basin. J. Geophys. Res., 100, 20665–20679, https://doi.org/10.1029/94JC01182.
- ——, A. J. Watson, and C. S. Law, 1998: Mixing of a tracer in the pycnocline. J. Geophys. Res., 103, 21499–21529, https://doi. org/10.1029/98JC01738.
- —, E. T. Montgomery, K. L. Polzin, L. C. St. Laurent, R. W. Schmitt, and J. M. Toole, 2000: Evidence for enhanced mixing over rough topography in the abyssal ocean. *Nature*, 403, 179–182, https://doi.org/10.1038/35003164.
- —, T. F. Duda, M. A. Sundermeyer, and H. E. Seim, 2004: Mixing in a coastal environment: 1. A view from dye dispersion. *J. Geophys. Res.*, 109, C10013, https://doi.org/10.1029/2003JC002194.
- —, R. He, Z. Xue, S. F. DiMarco, L. J. Spencer, and P. Chapman, 2016: Dispersion of a tracer in the deep Gulf of Mexico. *J. Geophys. Res. Oceans*, **121**, 1110–1132, https://doi.org/10.1002/2015JC011405.
- Lele, R., and Coauthors, 2021: Abyssal heat budget in the southwest Pacific basin. *J. Phys. Oceanogr.*, **51**, 3317–3333, https://doi.org/10.1175/JPO-D-21-0045.1.
- Lumpkin, R., and K. Speer, 2007: Global ocean meridional overturning. J. Phys. Oceanogr., 37, 2550–2562, https://doi.org/10. 1175/JPO3130.1.
- Mackay, N., J. R. Ledwell, M.-J. Messias, A. C. N. Garabato, J. A. Brearley, A. J. S. Meijers, D. C. Jones, and A. J. Watson, 2018: Diapycnal mixing in the Southern Ocean diagnosed using the DIMES tracer and realistic velocity fields. J.

- Geophys. Res. Oceans, 123, 2615–2634, https://doi.org/10.1002/2017JC013536.
- MacKinnon, J. A., and Coauthors, 2017: Climate process team on internal wave–driven ocean mixing. *Bull. Amer. Meteor. Soc.*, 98, 2429–2454, https://doi.org/10.1175/BAMS-D-16-0030.1.
- Marshall, J., C. Hill, L. Perelman, and A. Adcroft, 1997: Hydrostatic, quasi-hydrostatic, and nonhydrostatic ocean modeling. J. Geophys. Res., 102, 5733–5752, https://doi.org/10.1029/96JC02776.
- —, D. Jamous, and J. Nilsson, 1999: Reconciling thermodynamic and dynamic methods of computation of water-mass transformation rates. *Deep-Sea Res. I*, 46, 545–572, https://doi. org/10.1016/S0967-0637(98)00082-X.
- Mashayek, A., R. Ferrari, S. Merrifield, J. R. Ledwell, L. St Laurent, and A. N. Garabato, 2017: Topographic enhancement of vertical turbulent mixing in the Southern Ocean. *Nat. Commun.*, 8, 14197, https://doi.org/10.1038/ncomms14197.
- —, C. P. Caulfield, and M. H. Alford, 2021: Goldilocks mixing in oceanic shear-induced turbulent overturns. *J. Fluid Mech.*, 928, A1, https://doi.org/10.1017/jfm.2021.740.
- McDougall, T. J., and R. Ferrari, 2017: Abyssal upwelling and downwelling driven by near-boundary mixing. J. Phys. Oceanogr., 47, 261–283, https://doi.org/10.1175/JPO-D-16-0082.1.
- McWilliams, J. C., 2016: Submesoscale currents in the ocean. Proc. Roy. Soc., 472A, 20160117, https://doi.org/10.1098/rspa. 2016.0117.
- Munk, W. H., 1966: Abyssal recipes. Deep-Sea Res. Oceanogr. Abstr., 13, 707–730, https://doi.org/10.1016/0011-7471(66) 90602-4.
- —, and C. Wunsch, 1998: Abyssal recipes II: Energetics of tidal and wind mixing. *Deep-Sea Res. I*, **45**, 1977–2010, https://doi. org/10.1016/S0967-0637(98)00070-3.
- Nazarian, R. H., C. M. Burns, S. Legg, M. C. Buijsman, H. Kaur, and B. K. Arbic, 2021: On the magnitude of canyon-induced mixing. *J. Geophys. Res. Oceans*, 126, e2021JC017671, https://doi.org/10.1029/2021JC017671.
- Nikurashin, M., and R. Ferrari, 2010: Radiation and dissipation of internal waves generated by geostrophic motions impinging on small-scale topography: Theory. *J. Phys. Oceanogr.*, 40, 1055–1074, https://doi.org/10.1175/2009JPO4199.1.
- —, and S. Legg, 2011: A mechanism for local dissipation of internal tides generated at rough topography. *J. Phys. Oceanogr.*, 41, 378–395, https://doi.org/10.1175/2010JPO4522.1.
- Osborn, T. R., 1980: Estimates of the local rate of vertical diffusion from dissipation measurements. *J. Phys. Oceanogr.*, **10**, 83–89, https://doi.org/10.1175/1520-0485(1980)010<0083: EOTLRO>2.0.CO;2.
- —, and C. S. Cox, 1972: Oceanic fine structure. *Geophys. Fluid Dyn.*, **3**, 321–345, https://doi.org/10.1080/03091927208236085.
- Polzin, K. L., 2009: An abyssal recipe. *Ocean Modell.*, 30, 298–309, https://doi.org/10.1016/j.ocemod.2009.07.006.
- —, and T. J. McDougall, 2022: Mixing at the ocean's bottom boundary. *Ocean Mixing*, M. Meredith and A. Naveira Garabato, Eds., Elsevier, 145–180, https://doi.org/10.1016/ B978-0-12-821512-8.00014-1.
- —, J. M. Toole, and R. W. Schmitt, 1995: Finescale parameterizations of turbulent dissipation. J. Phys. Oceanogr., 25, 306–328, https://doi.org/10.1175/1520-0485(1995)025<0306: FPOTD>2.0.CO;2.
- —, —, J. R. Ledwell, and R. W. Schmitt, 1997: Spatial variability of turbulent mixing in the spatial variability abyssal ocean. *Science*, 276, 93–96, https://doi.org/10.1126/science.276. 5309.93.

- —, B. Wang, Z. Wang, F. Thwaites, and A. J. Williams, 2021: Moored flux and dissipation estimates from the northern deepwater Gulf of Mexico. *Fluids*, **6**, 237, https://doi.org/10.3390/fluids6070237.
- Ruan, X., and J. Callies, 2020: Mixing-driven mean flows and sub-mesoscale eddies over mid-ocean ridge flanks and fracture zone canyons. *J. Phys. Oceanogr.*, 50, 175–195, https://doi.org/10.1175/JPO-D-19-0174.1.
- —, and R. Ferrari, 2021: Diagnosing diapycnal mixing from passive tracers. J. Phys. Oceanogr., 51, 757–767, https://doi.org/10.1175/JPO-D-20-0194.1.
- Simmons, H. L., S. R. Jayne, L. C. St. Laurent, and A. J. Weaver, 2004: Tidally driven mixing in a numerical model of the ocean general circulation. *Ocean Modell.*, 6, 245–263, https:// doi.org/10.1016/S1463-5003(03)00011-8.
- Spingys, C. P., A. C. N. Garabato, S. Legg, K. L. Polzin, E. P. Abrahamsen, C. E. Buckingham, A. Forryan, and E. E. Frajka-Williams, 2021: Mixing and transformation in a deep western boundary current: A case study. *J. Phys. Oceanogr.*, 51, 1205–1222, https://doi.org/10.1175/JPO-D-20-0132.1.
- St. Laurent, L. C., and R. W. Schmitt, 1999: The contribution of salt fingers to vertical mixing in the North Atlantic tracer release experiment. J. Phys. Oceanogr., 29, 1404–1424, https:// doi.org/10.1175/1520-0485(1999)029<1404:TCOSFT>2.0.CO;2.
- —, J. M. Toole, and R. W. Schmitt, 2001: Buoyancy forcing by turbulence above rough topography in the abyssal Brazil basin. *J. Phys. Oceanogr.*, **31**, 3476–3495, https://doi.org/10.1175/1520-0485(2001)031<3476:BFBTAR>2.0.CO;2.
- Stommel, H., and A. B. Arons, 1959: On the abyssal circulation of the world ocean II. An idealized model of the circulation pattern and amplitude in oceanic basins. *Deep-Sea Res.*, 6, 217–233, https://doi.org/10.1016/0146-6313(59)90075-9.
- Sundermeyer, M. A., E. A. Terray, J. R. Ledwell, A. G. Cunningham, P. E. LaRocque, J. Banic, and W. J. Lillycrop, 2007: Threedimensional mapping of fluorescent dye using a scanning, depth-resolving airborne lidar. *J. Atmos. Oceanic Technol.*, 24, 1050–1065, https://doi.org/10.1175/JTECH2027.1.
- Talley, L. D., 2013: Closure of the global overturning circulation through the Indian, Pacific, and Southern Oceans: Schematics and transports. Oceanography, 26, 80–97, https://doi.org/10. 5670/oceanog.2013.07.
- Taylor, G. I., 1922: Diffusion by continuous movements. Proc. London Math. Soc., s2–20, 196–212, https://doi.org/10.1112/ plms/s2-20.1.196.
- —, 1953: Dispersion of soluble matter in solvent flowing slowly through a tube. *Proc. Roy. Soc. London*, **A219**, 186–203, https://royalsocietypublishing.org/doi/10.1098/rspa.1953.0139.
- Taylor, J. R., S. M. B. Kops, C. P. Caulfield, and P. F. Linden, 2019: Testing the assumptions underlying ocean mixing methodologies using direct numerical simulations. *J. Phys. Ocean*ogr., 49, 2761–2779, https://doi.org/10.1175/JPO-D-19-0033.1.
- Thorpe, S. A., 1977: Turbulence and mixing in a Scottish loch. Philos. Trans. Roy. Soc., A286, 125–181, https://doi.org/10. 1098/rsta.1977.0112.
- Thurnherr, A. M., L. C. St. Laurent, K. G. Speer, J. M. Toole, and J. R. Ledwell, 2005: Mixing associated with sills in a

- canyon on the midocean ridge flank. *J. Phys. Oceanogr.*, **35**, 1370–1381, https://doi.org/10.1175/JPO2773.1.
- —, L. Clément, L. S. Laurent, R. Ferrari, and T. Ijichi, 2020: Transformation and upwelling of bottom water in fracture zone valleys. *J. Phys. Oceanogr.*, **50**, 715–726, https://doi.org/ 10.1175/JPO-D-19-0021.1.
- Tozer, B., D. T. Sandwell, W. H. F. Smith, C. Olson, J. R. Beale, and P. Wessel, 2019: Global bathymetry and topography at 15 arc sec: SRTM15+. Earth Space Sci., 6, 1847–1864, https://doi.org/10.1029/2019EA000658.
- Trossman, D., C. B. Whalen, T. W. N. Haine, A. F. Waterhouse, A. T. Nguyen, A. Bigdeli, M. Mazloff, and P. Heimbach, 2022: Tracer and observationally derived constraints on diapycnal diffusivities in an ocean state estimate. *Ocean Sci.*, 18, 729–759, https://doi.org/10.5194/os-18-729-2022.
- Tulloch, R., and Coauthors, 2014: Direct estimate of lateral eddy diffusivity upstream of Drake Passage. J. Phys. Oceanogr., 44, 2593–2616, https://doi.org/10.1175/JPO-D-13-0120.1.
- Visbeck, M., M. Dengler, T. S. Tanhua, and M. Freund, 2020: Mixing and upwelling dynamics along the continental slope off Peru inferred from tracer release, hydrographic and microstructure measurements. *Ocean Sciences Meeting*, San Diego, CA, Amer. Geophys. Union, PS53A-03, https://agu. confex.com/agu/osm20/meetingapp.cgi/Paper/651229.
- Wagner, G. L., G. Flierl, R. Ferrari, G. Voet, G. S. Carter, M. H. Alford, and J. B. Girton, 2019: Squeeze dispersion and the effective diapycnal diffusivity of oceanic tracers. *Geophys. Res. Lett.*, 46, 5378–5386, https://doi.org/10.1029/2019GL082458.
- Walin, G., 1982: On the relation between sea-surface heat flow and thermal circulation in the ocean. *Tellus*, 34A, 187–195, https://doi.org/10.3402/tellusa.v34i2.10801.
- Waterhouse, A. F., and Coauthors, 2014: Global patterns of diapycnal mixing from measurements of the turbulent dissipation rate. J. Phys. Oceanogr., 44, 1854–1872, https://doi.org/10.1175/JPO-D-13-0104.1.
- Watson, A. J., and J. R. Ledwell, 1988: Purposefully released tracers. *Philos. Trans. Roy. Soc. London*, A325, 189–200, https://doi.org/10.1098/rsta.1988.0051.
- —, —, M.-J. Messias, B. A. King, N. Mackay, M. P. Meredith, B. Mills, and A. C. Naveira Garabato, 2013: Rapid crossdensity ocean mixing at mid-depths in the Drake Passage measured by tracer release. *Nature*, **501**, 408–411, https://doi. org/10.1038/nature12432.
- Wenegrat, J. O., J. Callies, and L. N. Thomas, 2018: Submesoscale baroclinic instability in the bottom boundary layer. J. Phys. Oceanogr., 48, 2571–2592, https://doi.org/10.1175/JPO-D-17-0264.1.
- Whalen, C. B., 2021: Best practices for comparing ocean turbulence measurements across spatiotemporal scales. *J. Atmos. Oceanic Technol.*, **38**, 837–841, https://doi.org/10.1175/JTECH-D-20-0175.1.
- —, C. de Lavergne, A. C. Naveira Garabato, J. M. Klymak, J. A. MacKinnon, and K. L. Sheen, 2020: Internal wave-driven mixing: Governing processes and consequences for climate. *Nat. Rev. Earth Environ.*, 1, 606–621, https://doi.org/10.1038/s43017-020-0097-z.